[American Journal of Science, Vol. 314, February, 2014, P. 462–507, DOI 10.2475/02.2014.02]

THE KATHERINA RING COMPLEX (SINAI PENINSULA, EGYPT): SEQUENCE OF EMPLACEMENT AND PETROGENESIS

M. EYAL*, A. N. ZANVILEVICH*, B. A. LITVINOVSKY*,†, B. M. JAHN**, Ye. VAPNIK*, and Y. BE'ERI-SHLEVIN***

ABSTRACT. The Katherina Ring Complex (KRC) in the central Sinai Peninsula, Egypt, was formed in three consecutive stages: volcanic, subvolcanic, and plutonic. The outer Katherina ring dike, about 30 km in diameter, marks the contour of a paleocaldera. Volcanic ignimbrite extrusions representing the earliest stage of the KRC were followed by emplacement of subvolcanic peralkaline microgranite bodies. The ring dikes are composed mainly of porphyritic quartz monzonite and plagioclase-rich quartz syenite, with less abundant alkali feldspar quartz syenite and peralkaline granite. The central alkaline granite pluton (*ca.* 210 km^2) was emplaced at ~595 Ma. The quartz monzonite–syenite group is characterized by positive Eu anomalies (Eu/Eu* = 1.1-1.6), which is consistent with its enrichment in accumulated plagioclase crystals (xenocrysts). These features, along with the positive $\varepsilon_{Nd}(T)$ values in quartz monzonite (up to +5.6) suggest that the initial silicic magma was hybridized by plagiclase-rich mafic magma. Mineral geothermometry and melt inclusion studies point to the formation of the silicic magmas at high temperatures, up to 900 to 1000 °C. Oxygen and Sr-Nd isotope data suggest that the source of the magmas was moderately depleted mantle or young juvenile crust. The trend of compositional change from quartz alkali feldspar syenite to alkali feldspar and peralkaline granite is consistent with a fractional crystallization model. A specific feature of the magma differentiation process is that the residual melt separation could occur when the magma was ~55 percent crystallized ("rigid percolation threshold") and clusters of crystals formed a rigid skeleton in the magma. At this stage, residual melt flowed pervasively through the pore space. The suggested model of melt separation alleviates the problem of a differentiation process since it does not require crystal settling that seems unrealistic in highly viscous silicic magmas at shallow depth. Chemical and Nd isotopic distinctions between the leucocratic volcanic–subvolcanic rocks ($\varepsilon_{Nd}(T)$ = 4.2-4.6) and the Katherina pluton granite (2.6-3.9) suggest that the silicic magmas of the volcanic-subvolcanic and the plutonic stages were probably produced from different mantle-derived sources.

Key words: Igneous ring complex, alkaline and peralkaline granite, ring dike, hybridization, fractional crystallization, Sinai Peninsula

INTRODUCTION

Ring complexes and associated igneous rocks are abundant throughout Africa and Arabia. Of them, 154 Neoproterozoic complexes, mostly with incorporated alkali granitoids, occur in the Arabian-Nubian Shield (ANS) (Vail, 1989). The close association in time and space of successive volcanic rocks, ring dikes and plutonic rocks provides a unique opportunity for studying the evolution of magma sources and processes of magma generation, interaction, and mixing. The ring complexes in the ANS were extensively studied till the late 1980's (Vail, 1989 and references therein). Since then, systematic studies of the ring complexes became rare (for example, Harris, 1985; Küster, Harms, 1998; Moghazi and others, 2011).

* Department of Geological and Environmental Sciences, Ben-Gurion University of the Negev, Beer-Sheva 84105, Israel
** Department of Geosciences, National Taiwan University, P.O. Box 13-318 Taipei 106, Taiwan
*** Institute of Earth Sciences, Hebrew University of Jerusalem, Jerusalem 91904, Israel
† Corresponding author: litboris@gmail.com

In the central part of the Sinai Peninsula (Egypt) two typical ring complexes, Iqna and Katherina, are known since 1980 (Eyal and others, 1980). The Late Neoproterozoic Katherina Ring Complex (KRC) has been studied in detail recently (Eyal and others, 2010; Farahat and Azer, 2011; Moreno and others, 2012). Along with numerous A-type granite plutons of Sinai, southern Israel and SW Jordan, the KRC was formed during the last stage of the ANS evolution in a intracontinental tectonic setting, when a fundamental transition in tectonic style, from compressional to extensional, occurred 610 to 590 My ago (Gass, 1982; Stern and others, 1984; Bentor, 1985; Kröner and others, 1987; Stern, 1994; Genna and others, 2002; Meert, 2003; Jarrar and others, 2003, 2008; Be'eri-Shlevin and others, 2009a). In the previous work (Katzir and others, 2007) we described the central Katherina granite pluton and discussed the nature of its vertical zoning. In this paper, we discuss the structure, geological history and petrogenesis of the whole Katherina Ring Complex. Furthermore, we emphasize the role of fractional crystallization and magma mixing in the formation of heterogeneous quartz monzonite–syenite and associated silicic rocks, which make up large ring dikes and numerous subvolcanic intrusive bodies within the KRC.

GEOLOGICAL SETTING

The first detailed geological mapping of the Katherina Ring Complex was carried out by Y. K. Bentor and M. Eyal. Subsequently, M. Eyal studied the vertical zoning of the Katherina pluton (Eyal and Hezkiyahu, 1980) and supervised two Ms theses, including Goor (ms, 1982) on the volcanic rocks, Inner Ring Dike and related units, and Bruner (ms, 1982) on the Outer Ring Dike. Farahat and Azer (2011) studied the Gebel Tarbush area (north-western part of the KRC); their data on main rock types, mineral chemistry and elemental geochemistry are in good consistency with the data for the Complex as presented below.

The KRC is situated in the high mountainous area of the Sinai crystalline basement (fig. 1). Gebel Musa, traditionally believed to be the biblical Mt. Sinai, is located in the central part of the complex. Structurally the exposed area is a big caldera eroded to its roots. The erosion almost entirely eliminated the volcanic edifice and exposed the alkaline granite pluton and the basement country rocks. The size (400 km^2) and elliptical shape of the caldera (26.5 km by 16.5 km) are delineated by the Outer Ring Dike (fig. 1).

Three main stages of the Complex formation are recognized: (1) The volcanic stage represented by the Jarjaniya Formation, which corresponds to the term Katherina volcanics in the works of Egyptian geologists. (2) The subvolcanic stage comprises peralkaline porphyritic microgranite intrusions, the porphyritic quartz monzonite intrusion, two ring dikes of complex composition, and scattered perthite quartz syenite dikes. (3) The Katherina alkaline granite pluton was emplaced at the final stage of the KRC formation.

Volcanic Rocks of the Jarjaniya Formation

At the present level of exposure only several volcanic relicts, overlying with angular unconformity the eroded Rutig Formation, are retained in the central and western parts of the caldera (fig. 1). The best studied volcanic section of 2 km^2 in area and about 350 m thick crops out in the central part of the caldera (fig. 2). It comprises rhyolitic ignimbrite, volcanic breccia and peralkaline ignimbrite. Flows of rhyolitic ignimbrite ~130 m thick, the oldest exposed rock type of the KRC, form the base of the volcanic section. Volcanic breccia composed of angular rock fragments, 0.5 to 40 cm in size, embedded in crystal rich rhyolite tuff, makes up a 200 m thick section overlying the rhyolitic ignimbrite. Peralkaline ignimbrite, about 50 m thick, builds the upper part of the section east of the Gebel Katherina peak. Both lower and upper ignimbrites dip 20 to 30° to the west as measured on the orientated pumice.

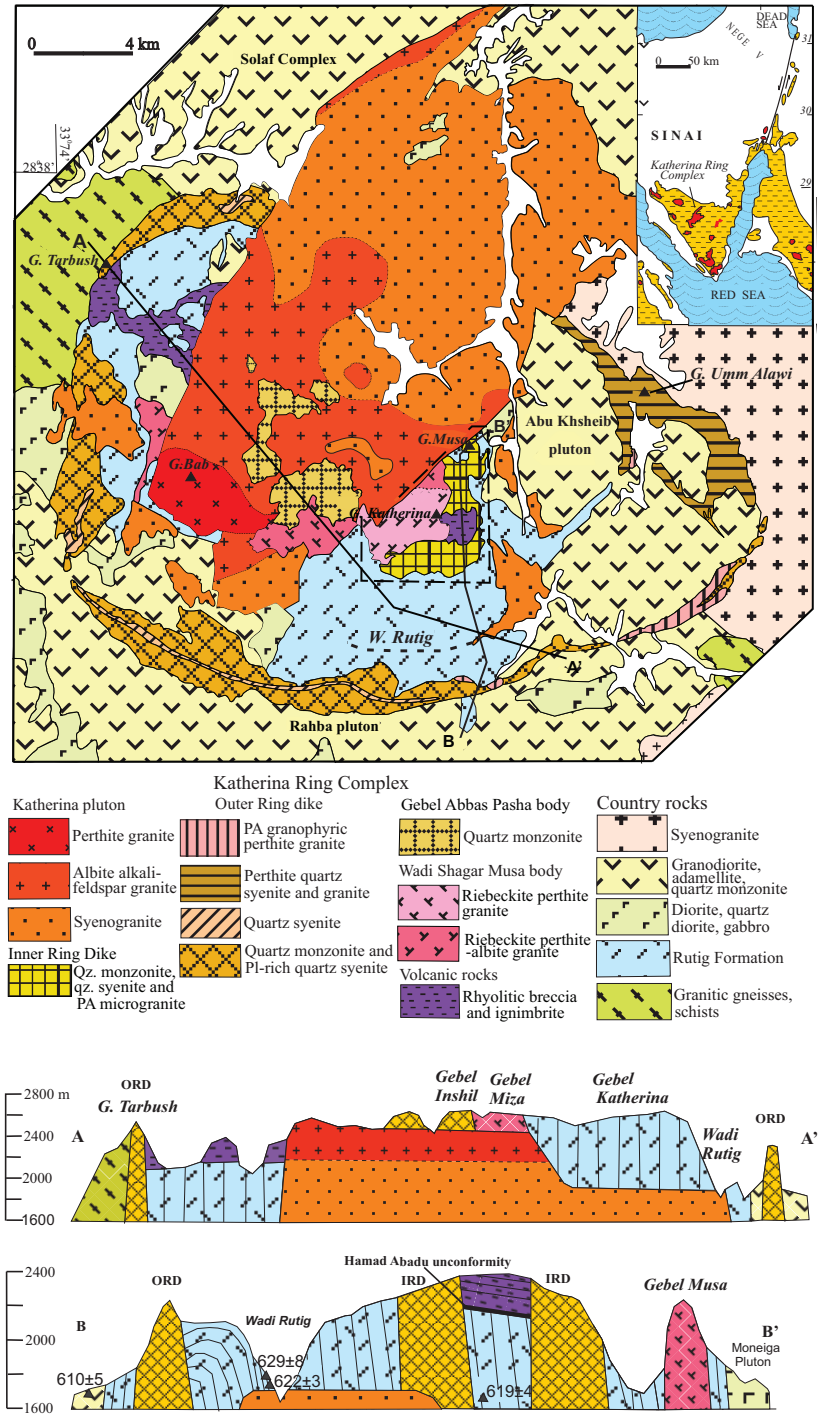

Fig. 1. Schematic geological map and cross sections AA′ and BB′ of the Katherina Ring Complex. *Inset*: Location of the Katherina Ring Complex and related alkaline granite plutons in Sinai Peninsula and adjacent areas. Contour in the central part outlines the area shown in figure 2. Symbols in cross sections are the same as in the map. IRD, Inner Ring Dike; ORD, Outer Ring Dike.

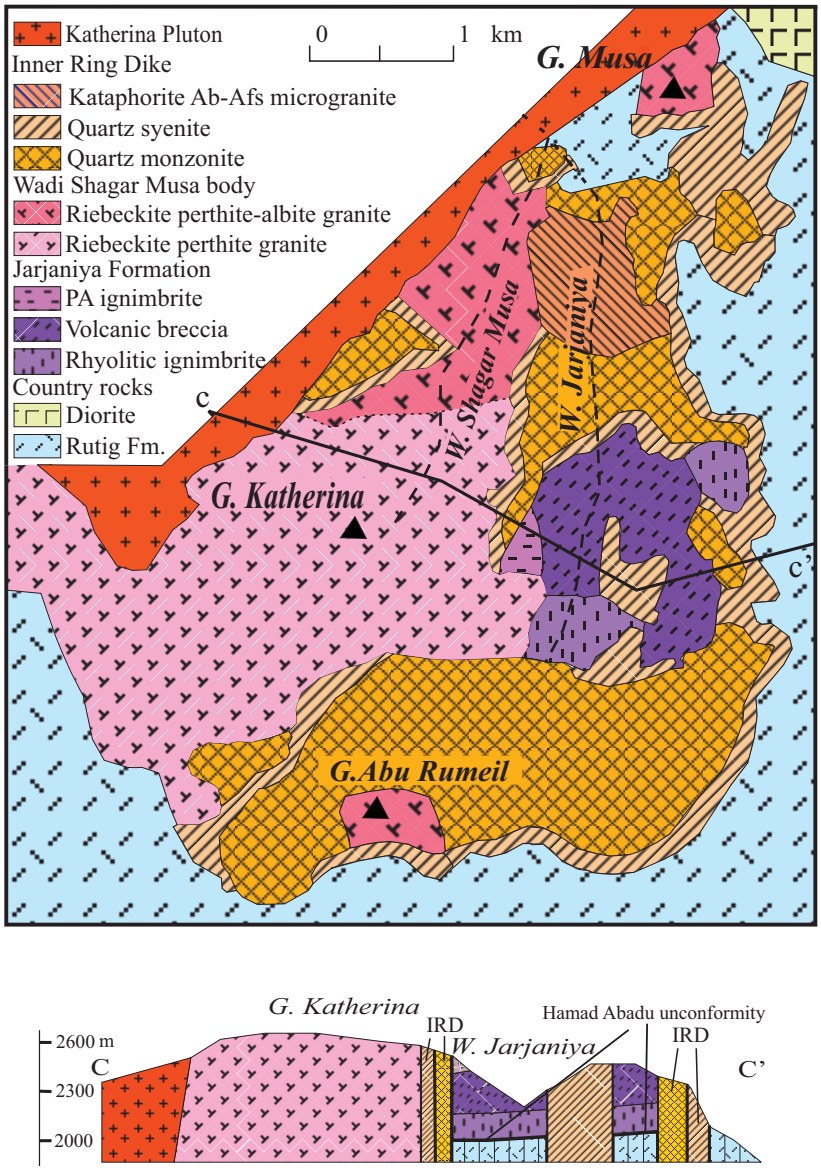

Fig. 2. Schematic geological map and cross section CC′ of the central part of the caldera illustrating more details in the Inner Ring Dike area (Gebel Katherina and vicinity).

Subvolcanic Intrusions

Within the subvolcanic stage, three successive sub-stages are distinguished: (1) emplacement of peralkaline granite (Wadi Shagar Musa, Gebel Musa and Gebel Abu Rumeil intrusives and necks); (2) formation of quartz monzonite–Pl-rich quartz syenite intrusive bodies (Abbas Pasha), Inner Ring Dike (IRD) and Outer Ring Dike (ORD); (3) emplacement of perthite quartz syenite and perthite granite magmas, crystallized as small bodies within the IRD and ORD and as dikes in the central part of the caldera.

Wadi Shagar Musa subvolcanic intrusion.—The body is located in the central part of the caldera. The exposed area is ~15 km^2, ranging between 1700 m and 2644 m in altitude (highest point in Sinai, summit of Gebel Katherina (fig. 1). It is made up of riebeckite–arfvedsonite porphyritic microgranite, which is perthitic in the upper part and changes gradually downwards in the pluton to the two-feldspar (albite and perthite) granite over a distance of a few tens of meters. The peralkaline porphyritic microgranite intrudes the Rutig and Jarjaniya formations and is intruded by the quartz monzonite of the younger intrusions. West of Gebel Katherina the body is intruded by the Katherina pluton with sharp subvertical contacts, whereas at Gebel Miza the contact surface between the subvolcanic roof pendant and the Katherina pluton, though also intrusive, is subhorisontal and flat (fig. 1, cross section AA′).

The Gebel Musa and Gebel Abu Rumeil peralkaline porphyritic microgranite necks.—The Gebel Musa body is ~0.3 km^2 in area. It intrudes the volcano-sedimentary rocks of the Rutig Formation and is intruded by perthite quartz syenite of the IRD and by the Katherina pluton. The rocks are riebekite two-feldspar porphyritic microgranite. Vertical lineation of riebeckite crystals at the peak of Gebel Musa is interpreted as evidence of magma flow in a volcanic neck. The Gebel Abu Rumeil (fig. 2) body is similar to the Gebel Musa in its size, composition, and relationships with country rocks.

The Gebel Abbas Pasha subvolcanic intrusion.—It comprises three closely spaced roof pendants of the Katherina pluton, composed of quartz monzonite and Pl-rich quartz syenite. The roof pendants are probably the relicts of a single much larger body (fig. 1 and cross section AA′). Their present total area is ~14 km^2. The Gebel Abbas Pasha body intrudes the Wadi Shagar Musa peralkaline porphyritic microgranite.

The Inner Ring Dike.—The dike is located in the vicinity of the caldera center, to the south of Gebel Musa (figs. 1 and 2). It has a semicircular shape, with an exposed length of ~11 km. Its width varies from a few meters to ~1250 m, and vertical exposure attains 800 m. The northwestern part of the dike is cut by the Katherina pluton. The IRD was emplaced in three phases. The early phase is dominated (~90%) by quartz monzonite and Pl-rich quartz syenite similar to the main rock type of the Gebel Abbas Pasha intrusion. This phase intrudes with sharp and subvertical contacts the Rutig Formation, the Jarjaniya volcanics, and the Wadi Shagar Musa peralkaline porphyritic microgranite. Quartz syenite of the second phase forms two dikes several meters wide along both sides of the quartz monzonite body with sharp and vertical contacts. The kataphorite Ab-Afs microgranite marks the third phase of intrusion. It makes up a body of about 1 km^2 in area in the northern part of Wadi Jarjaniya (fig. 2).

Quartz syenite dikes.—They intrude all rock units of the central part of the caldera except the ORD and the Katherina pluton. The dikes are vertical, generally with a width of a few meters, although in places (at the vicinity of Gebel Musa) they are several tens of meters wide (fig. 2). Red color and coarse grained texture make them distinctive in the field. Quartz syenite occurs also as enclaves, from a few tens of cm to a few tens of meters, in the quartz monzonite variants of the IRD and Gebel Abbas Pasha intrusion.

The Outer Ring Dike (ORD).—This dike was emplaced along a circular fault that outlines the KRC caldera (Eyal and others, 1980). It is prominent in the landscape with its higher elevation and brown color. The length of the dike is 79 km, the width ranges from a few meters to 2.5 km. The maximum range of altitude is 1900 m. The contacts with country rocks are always sharp, and both inner and outer contacts dip inward 60 to 85°. The ORD was emplaced in three phases: (1) quartz monzonite, (2) quartz syenite and granite, and (3) perthite quartz syenite, granite and peralkaline granite.

Quartz monzonite is the dominant rock type in the ORD making up its western and southern parts (fig. 1). It forms a rocky cliff in a black landscape. The chilled zone along both sides of the dike (~1 m to 10 meters) is exhibited by microcrystalline to

fine-grained rocks followed by porphyritic quartz monzonite with very fine-grained matrix.

Quartz syenite with secondary granite is located in the southern part of the ORD forming a continuous dike-like subvertical body about 20 km long and from a few meters to ~250 m wide within the central part of the ring dike (fig. 1). In many places at the outer sides of this body an alternation of strips 3 to 6 m wide of porphyritic quartz monzonite and quartz syenite with vertical sharp and gradational contacts is abundant.

Perthite quartz syenite, granite and peralkaline granite constitute the eastern part of the ORD (fig. 1), whereas in the other parts of the ring dike they form strips of brown to light red rocks, coarse grained in appearance, a few meters to ~50 meters thick. They intrude the porphyritic quartz monzonite and porphyritic quartz syenite with a sharp contact, chilling zone and apophyses. Such field relations attest that the alkaline and peralkaline quartz syenite and granite of the ORD are younger than peralkaline microgranite emplaced at the beginning of the subvolcanic stage.

Plutonic Stage

The Katherina pluton.—The Katherina pluton, about 210 km^2 in area, is oriented SSW–NNE, crossing the northern border of the caldera (fig. 1). However, about 75 percent of the pluton area is located within the caldera, where the granite intrudes all other rocks of the KRC. At the northern end, the pluton intrudes the country rocks as a dike >1 km wide, that narrows gradually over a distance of 20 km into a horse-tail splay of small dikes, each about 5 to 10 m wide. The pluton has a fairly flat upper surface dipping north about 5° and steeply dipping walls (Eyal and Hezkiyahu, 1980). The contact of granite with country rocks is sharp, with a zone of pegmatites and aplites a few tens of meters wide. Due to the flat upper surface of the pluton, the contact between granite and earlier subvolcanic roof pendants (Abbas Pasha and western part of Wadi Shagar Musa intrusives) is subhorizontal and flat (fig. 1, cross section AA′). Satellite outcrops of the pluton occur in Wadi Rutig, where the contact of granite with the Rutig Formation is flat (fig. 1, cross section BB′) and near the western pluton margin where the contact is steeply dipping. Vertical compositional zoning in the pluton was established by a detailed mapping, sampling and petrographic study of large polished slabs (Eyal and Hezkiyahu, 1980). The results show that the bulk of the pluton is made up of syenogranite, whereas the highest parts of the pluton (the Gebel Bab area in its SW part) consist of perthite granite. The maximum thickness of the perthite granite zone is more than 500 m. The 300 to 500 m thick zone below the perthite granite is made up of two-feldspar (albite and alkali feldspar, or Ab-Afs) granite. The transition from syenogranite to Ab-Afs granite is barely discernible in outcrops and recognized only by the decrease in plagioclase content (approximately ≤20 vol. %) and change of the latter composition from oligoclase to albite. The contact between the Ab-Afs and perthite granite is also gradational, and it becomes more distinguishable due to the color contrast with the redder perthite granite (Eyal and Hezkiyahu, 1980; Katzir and others, 2007).

The Basement Country Rocks

The basement country rocks within the caldera comprise the volcano-sedimentary Rutig Formation and calc-alkaline diorite and granitoid bodies that intruded the Rutig rocks.

The Rutig Formation.—These rocks are exposed in the southern and western parts of the caldera (fig. 1). The best-studied area, about 8 km long, is located between Wadi Rutig to the south and Gebel Musa to the north. Over this area the volcano-sedimentary succession of the Rutig Formation strikes approximately E-W and the dip is 40 to 90° due N (fig. 1, cross section BB′). The structure is an antiform with an E-W horizontal axis located in the southernmost area, between the Wadi Rutig and the

ORD. The antiform structure can be clearly seen from the high above in the uppermost part of Wadi Rutig. The thickness of the section is 6 to 7 km; the base is located near Gebel Musa, where the rocks show evidence of low-grade metamorphism, and the top occurs at the horizontal axis where no sign of metamorphism is observed. These data prove that the structure is an overturned syncline. The gently dipping volcanic rocks of the Jarjaniya Formation overlay the lower part of eroded Rutig Formation with angular unconformity. This suggests deep erosion of more than 6 km of the Rutig sequence. The erosion decreases due south, toward the axis of the antiform. The extensive folding followed by intrusion of calc-alkaline granitoid plutons and significant erosion of the Rutig sequence that preceded the early volcanic stage of the KRC indicate that the Rutig formation cannot be regarded as part of the Complex as suggested by some workers (for example, Moreno and others, 2012).

Calc-alkaline plutonic rocks.—The diorite and quartz diorite intrusions make up a few intrusive bodies covering less than 1 km^2, located immediately north-east of Gebel Musa (Moneiga body, fig. 2), southwest and west of the Katherina pluton, and as roof pendants in its northern part. The Moneiga quartz diorite intrudes the Rutig Formation. The granitoids constitute the Abu Khsheib quartz monzonite pluton located in the eastern part of the ring complex and one more granodiorite pluton sited between the Abu Khsheib and the Rutig Formation (fig. 1).

The basement rocks exposed immediately outside the caldera comprise the eastern part of the Feiran-Solaf Metamorphic Complex at the NW, the calc-alkaline granitoid complexes, Solaf in the north, the calc-alkaline Rahba granodiorite pluton in the south and several smaller granitic plutons in the southeast, east and northeast (fig. 1). Concise characteristics of the plutons are given in Eyal and others (1980, 2010).

PETROGRAPHY AND MINERAL CHEMISTRY

Volcanic Rocks of the Jarjaniya Formation

Rhyolitic ignimbrite is a dark gray to dark brown rock, composed of broken oligoclase phenocrysts (An_{10-15}, 10-16%), flattened pumice (<5 cm, 6-25%) and angular volcanic rock fragments (0.5-5 cm, 0-3%), embedded in a devitrified microcrystalline to fine grained matrix (64-74%), which consists of quartz, alkali feldspar and ore minerals.

Volcanic breccia of rhyolite composition comprises angular rock fragments of ignimbrite, spherolitic alkali rhyolite, vitrophyric quartz porphyry, trachyte, and granite. The matrix is a crystal rich rhyolite tuff consisting of microcrystalline quartz and alkali feldspar, with subhedral phenocrysts of oligoclase (An_{10-18}) and minor quartz.

Peralkaline ignimbrite is a black fluidal rhyolite porphyry with medium grained phenocrysts of perthite An_{0-1} Ab_{39-58} Or_{41-61}(10-15%) and quartz (5-10%). The *matrix* (~80%) is a devitrified glass consisting of quartz and alkali-feldspar, with flow oriented shards and flattened pumice 1 to 15 mm in length. Aegirine prisms occur in rounded clusters 3 mm in diameter and riebeckite as subhedral crystals 0.03 mm across. In some ignimbrite flows, rare prismatic plagioclase phenocrysts (An_{12-14}) are observed. Judging from the peralkaline rhyolite composition of glass in the matrix (table 6, microprobe analysis data), these are xenocrysts rather than phenocrysts.

Subvolcanic Intrusive Rocks

It follows from the foregoing chapter that subvolcanic rocks represent the most diverse group in the KRC. The AQP classification diagram (fig. 3A) based on the modal compositions of 62 samples (Online table 1-SD, http://earth.geology.yale.edu/~ajs/SupplementaryData/2013/04EyalSD-1.doc) demonstrates that the group incorporates peralkaline porphyritic microgranite, alkali feldspar quartz syenite and granite, quartz syenite and granite, and quartz monzonite. The perthite-quartz-albite

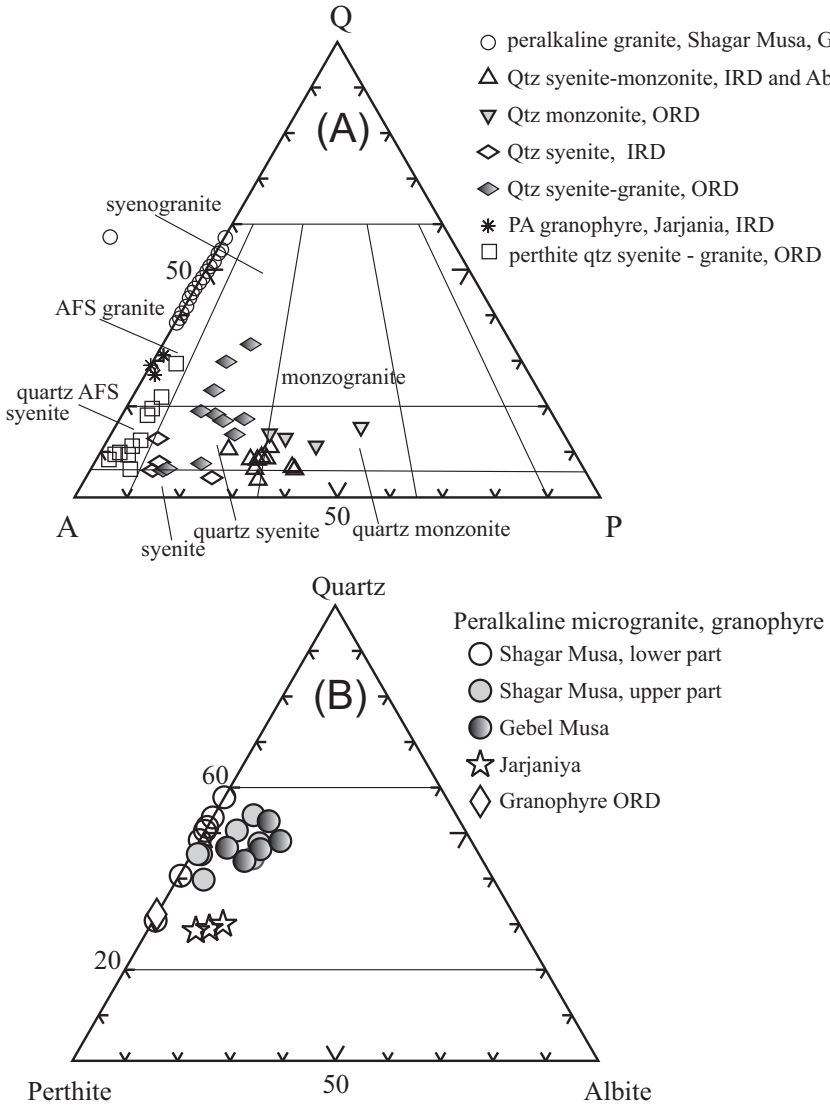

Fig. 3. Modal compositions of igneous rocks from the Katherina Ring Complex. (A) Classification AQP diagram. (B) Compositions of peralkaline porphyritic microgranite in the diagram "perthite-albite-quartz," illustrating distinctions between two peralkaline granite varieties, perthite (hypersolvus) and Ab-Afs (subsolvus).

diagram (fig. 3B) allows distinguishing the perthite and two feldspar (Ab-Afs) peralkaline granites (hypersolvus and subsolvus granites, respectively). The average modal compositions of the different rock types and their ranges are presented in table 1.

All subvolcanic rocks are porphyritic, with a fine grained to microcrystalline dark matrix (20-70%). Only in some of the perthite quartz syenite the amount of matrix decreases to 10 to 15 percent, whereas size of phenocrysts is 4 to 7 mm. Therefore this rock type seems to be coarse grained.

Peralkaline porphyritic microgranites comprise two varieties: perthite and two-feldspar (Ab-Afs). Riebeckite-perthite porphyritic microgranite makes up the upper part of the

TABLE 1

Modal compositions (averages and ranges) of subvolcanic rocks from the Katherina Ring Complex

Rock type	PA perth. granite		PA Ab-Afs granite				Quartz monzonite - Pl-rich quartz syenite						Perthite qtz syenite	
Intrusion	Wadi Shagar Musa				G. Musa		Abbas Pasha		IRD		ORD		ORD	
Mineral, vol.%	Av. (7)	Range	Av. (6)	Range	Av. (6)	Range	Av. (4)	Range	Av. (6)	Range	Av. (4)	Range	Av. (7)	Range
Quartz	45.9	36-53	43.4	37-51	43.1	41-45	7.7	7.1-9	5.3	3.1-9	11.5	9.3-13	11.5	9.2-17
Perthite	48.7	38-59	43.6	37-52	38.4	32-44	52.8	50-56	45.0	35-51	41.6	33-48	76.0	72-79
Albite	0.1	0-0.4	5.2	1-	10.4	5.4-								
Plagioclase							25.0	20-27	25.6	24-29	32.0	26-41	4.7	3-6.4
Riebeckite	2.9	0.7-7	3.4	0-8	6.1	2.3-9								
Aegirine	0.1	0-07	0.2	0-1	0.2	0-1.3							0.1	0-0.5
Hornblende							8.4	6.9-10	9.1	6-11.6	5.6	4.4-6	3.2	2.2-6
Pyroxene							0.3	0-0.8	1.8	0.8-	0.9	0-1.3		
Biotite			1.2	0-5	0.3	0-2	1.0	0.1-2	4.1	2.4-7	1.5	0.3-	1.0	0-2
Chlorite											1.4	0-3.3	0.4	0-1
Zircon	0.4	0-1	0.6	0-2	0.4	0-0.7	0.7	0.2-1	0.2	0-1	1.3	1-1.6	0.3	0.1-0.5
Sphene	0.1	0-0.3			0.1	0-0.3					0.4	0-1	0.2	0-1.5
Apatite	0.1	0-0.1					0.1	0.1-	1.0	0.6-	0.2	0.1-	0.2	0-0.6
Ore	1.8	1.1-3	2.5	0.7-5	1.0	0.5-2	3.9	2-4.9	7.9	4.8-13	3.9	2.3-7	2.3	1-2.2

Table 1
(continued)

Rock type	Quartz syenite								PA and AFS granite				
Intrusion	Shagar Musa		Abbas Pasha		IRD		ORD		Jarjaniya body		ORD		ORD
Mineral, vol.%	Av. (2)	Range	Av. (2)	Range	Av. (2)	Range	Av. (10)	Range	Av. (3)	Range	Av. (3)	Range	1
Quartz	5.1		5.3	3.6-7	8.6	5.3-12	16.1	6-27.6	25.7	25-26	20.9	18-25	31.5
Perthite	72.9	72-74	67.0	62-72	72.1	71.7-72.4	56.0	41-75	52.5	48-55	64.9	59-70	66.5
Albite									10.1	8.2-12			
Plagioclase	9.5	7.2-12	16.1	11.1-21	10.6	8.7-13	15.8	12.3-22			4.8	4.3-	
Riebeckite													
Aegirine													
Hornblende	6.6	6.2-7	8.2	6.7-10	5.9	4.7-7	5.5	2.3-11	5.4	4.5-7	5.5	4.7-	
Pyroxene	0.6	0-1	0.3	0-0.5			0.6	0-1.6					
Biotite	1.8	1.5-2	0.9	0.8-1	0.5	0.2-0.7	2.6	1-4.4	0.7	0.3-1.2	0.9	0.4-	
Chlorite							0.3	0-1.3			0.3	0-1	
Zircon	1.5	1-1.9	0.4	0.2-0.5	0.4	0.3-0.4	0.6	0.2-1	2.0	0.6-2	0.7	0.4-1	0.1
Sphene	0.3	0.3	0.4	0.3-0.5	0.4	0-0.8	0.2	0-0.6					
Apatite	0.2	0-0.3	0.2	0-0.3	0.4	0.2-0.6	0.2	0-0.8	0.1	0-0.2	0.1	0-0.3	
Ore	1.8	0.6-3	1.5	1.2-1.7	1.3	1.2-1.3	2.1	0.9-4	3.4	2.8-3.4	2.0	0.9-3	1.9

TABLE 2

Compositions of feldspars in main rock types of the volcanic and subvolcanic rocks from the Katherina Ring Complex (microprobe analysis, wt.%)

	Volcanic rocks		Wadi Shagar Musa				G. Musa	Inner Rind Dike					
Rock	PA rhyolite	Alk rhyolite	PA microgranite					Quartz monzonite - Pl-rich quartz syenite type					
Sample #	AG-41	AG-178	AG-150		AG-55		AG-57	AG-58					
Analysis	1	2	3	4	5	6	7	8	9	10	11	12	12
Feldspar	Afs Phenocr.	Pl Xenocr.	Afs Phenocr.	Afs Matrix	Afs Phenocr.	Afs Matrix	Afs Phenocr.	Pl phenocryst Core-1	Rim-1	TFS phenocryst Core-2*	Rim-2*	Afs Phenocr.	Matrix Afs
SiO_2	66.13	66.41	65.71	65.22	66.08	67.71	64.48	61.13	63.20	63.17	64.37	66.39	65.45
Al_2O_3	18.55	19.39	18.36	17.89	18.71	16.57	18.55	24.36	23.25	20.95	19.03	19.30	18.84
FeO*	0.39	0.23	0.28	0.49	0.40	0.84	0.86	0.38	0.49	0.45	0.32	0.22	0.39
CaO	-	3.40	-	-	0.13	0.04	0.06	5.51	4.33	2.14	1.21	0.54	0.14
Na_2O	4.49	10.67	5.83	3.61	6.66	4.01	5.11	8.26	8.75	7.53	6.14	5.80	3.65
K_2O	10.75	0.77	8.49	11.12	7.85	10.08	10.29	0.45	0.75	4.46	7.50	8.02	11.05
BaO	n.d.	n.d.	n.d.	n.d.	n.d.	n.d.	n.d.	n.d.	n.d.	n.d.	n.d.	n.d.	n.d.
Total	100.30	100.87	98.67	98.33	99.82	99.25	99.34	100.09	100.75	98.69	98.57	100.25	99.51
Atoms to 8 oxygens													
Si	2.996	2.918	3.001	3.015	2.984	3.081	2.988	2.717	2.784	2.867	2.948	2.977	2.987
Al	0.991	1.004	0.988	0.975	0.996	0.889	1.012	1.276	1.207	1.120	1.027	1.020	1.013
Fe	0.015	0.009	0.011	0.019	0.015	0.032	0.033	0.014	0.018	0.017	0.012	0.008	0.015
Ca	0.000	0.160	0.000	0.000	0.006	0.002	0.003	0.263	0.204	0.104	0.059	0.026	0.007
Na	0.394	0.909	0.516	0.324	0.583	0.354	0.459	0.712	0.747	0.663	0.545	0.504	0.323
K	0.621	0.043	0.494	0.656	0.452	0.586	0.608	0.025	0.042	0.258	0.438	0.459	0.643
Ba	n.d.	n.d.	n.d.	n.d.	n.d.	n.d.	n.d.	n.d.	n.d.	n.d.	n.d.	n.d.	n.d.
End members, mol.%													
An	0	14	0	0	1	0	0	26	21	10	6	3	1
Ab	39	82	51	33	56	38	43	71	75	65	52	51	33
Or	61	4	49	67	43	62	57	3	4	25	42	46	66

TABLE 2
(continued)

	Inner Rind Dike									Outer Rind Dike			
Rock	Quartz monzonite - Pl-rich quartz syenite type							PA granophyre		Qtz monzonite - Pl-rich quartz syenite type			
Sample #	AG-58					IL-88	B	AG-9		IL-69			
Analysis	14	15	16	17	18	19	20	21	22	23	24	25	26
Feldspar	Plg?	Pl phenocrysts			Afs	TFS phenocrysts		Afs	Afs	Pl-1	Pl & TFS phenocrysts		
	Pl-3	Core-3	Rim-3	Core-4	Rim-4	Center*	Center*	Phenocr.	Phenocr.	Phenocr.	core-5	rim-5*	core-6*
SiO_2	64.71	62.32	64.54	62.34	64.75	65.31	63.36	67.02	67.08	58.66	59.67	64.34	63.47
Al_2O_3	20.70	23.07	21.95	22.52	18.46	21.63	22.61	18.71	18.37	25.64	24.70	19.67	20.52
FeO*	0.89	0.39	0.35	0.40	0.21			0.30	0.35	0.28	0.39	0.38	0.39
CaO	2.63	4.48	3.24	4.32	0.29	2.34	3.61	0.05	-	7.37	6.33	1.53	2.11
Na_2O	9.31	8.63	9.38	8.80	3.08	7.81	8.36	5.75	5.03	7.32	7.63	7.25	7.33
K_2O	1.20	0.62	0.41	0.31	11.98	3.01	2.01	8.58	9.38	0.50	0.83	5.40	4.42
BaO	n.d.	n.d.	n.d.	n.d.	n.d.	n.d.	1.34	n.d.	n.d.	0.33	0.25	0.62	n.d.
Total	99.44	99.50	99.87	98.69	98.77	100.10	101.29	100.42	100.21	100.09	99.82	99.18	98.24
Atoms to 8 oxygens													
Si	2.891	2.778	2.851	2.797	2.987	2.878	2.816	3.004	3.019	2.630	2.680	2.917	2.886
Al	1.042	1.212	1.143	1.191	1.004	1.122	1.184	0.988	0.974	1.355	1.307	1.051	1.100
Fe	0.041	0.015	0.013	0.015	0.008			0.011	0.013	0.010	0.015	0.015	0.015
Ca	0.123	0.214	0.153	0.208	0.015	0.110	0.172	0.003	0.000	0.354	0.305	0.074	0.103
Na	0.813	0.746	0.804	0.766	0.275	0.667	0.721	0.500	0.439	0.636	0.665	0.637	0.646
K	0.245	0.035	0.023	0.018	0.705	0.169	0.114	0.490	0.538	0.029	0.048	0.312	0.257
Ba	n.d.	n.d.	n.d.	n.d.	n.d.	n.d.	0.023	n.d.	n.d.	0.006	0.004	0.011	n.d.
End members, mol.%													
An	14	22	16	21	2	12	17	1	0	35	30	7	10
Ab	82	74	82	77	28	71	72	50	45	62	65	62	64
Or	4	4	2	2	70	18	11	49	55	3	5	30	26

TABLE 2
(continued)

	Outer Rind Dike												
Rock	Qtz monzonite - Pl-rich quartz syenite type										Pl-rich quartz syenite		
Sample #	IL-69				IL-74						IL-167		
Analysis	27	28	29	30	31	32	33	34	35	36	37	38	39
Feldspar	Pl & TFS phenocrysts			Afs	Pl-1	Pl-2, Afs and TFS phenocrysts				Afs	Pl-1	Pl-2	Afs
	Rim-6	Core-7*	Rim-7*	Matrix	Phenocr.	Core-8	Rim-8	Core-9*	Rim-9	Matrix	Phenocr.	Phenocr.	Matrix
SiO_2	64.83	63.18	65.59	65.37	60.42	61.98	65.73	59.34	65.53	65.10	59.59	61.42	66.02
Al_2O_3	19.40	21.00	19.43	19.48	24.88	22.69	19.31	24.50	18.72	19.18	24.95	23.42	19.42
FeO*	1.43	0.45	0.58	0.37	0.17	0.30	0.21	0.32	0.51	0.32	0.51	0.38	0.22
CaO	0.91	2.30	1.83	0.67	6.45	4.32	0.57	6.59	0.38	0.83	7.08	4.74	0.47
Na_2O	6.05	7.15	6.68	5.80	7.86	8.38	5.54	7.45	7.02	6.56	7.55	8.03	6.94
K_2O	6.73	4.72	6.02	8.34	0.29	0.88	8.13	1.07	6.53	6.38	0.60	1.05	6.31
BaO	n.d.	n.d.	n.d.	0.46	0.13	1.07	0.48	0.26	0.52	0.41	0.35	0.77	0.24
Total	99.35	98.80	100.14	100.48	100.19	99.60	99.97	99.53	99.21	98.79	100.63	99.80	99.63
Atoms to 8 oxygens													
Si	2.938	2.866	2.936	2.949	2.688	2.785	2.969	2.676	2.976	2.959	2.659	2.754	2.969
Al	1.036	1.123	1.025	1.036	1.304	1.201	1.028	1.302	1.002	1.028	1.312	1.238	1.029
Fe	0.054	0.017	0.022	0.014	0.006	0.011	0.008	0.012	0.019	0.012	0.019	0.014	0.008
Ca	0.044	0.112	0.088	0.032	0.308	0.208	0.028	0.318	0.018	0.040	0.339	0.228	0.023
Na	0.532	0.629	0.579	0.507	0.678	0.730	0.485	0.651	0.618	0.578	0.653	0.698	0.605
K	0.389	0.273	0.344	0.480	0.016	0.051	0.468	0.062	0.378	0.370	0.034	0.060	0.362
Ba	n.d.	n.d.	n.d.	0.008	0.002	0.019	0.009	0.005	0.009	0.007	0.006	0.014	0.004
End members, mol.%													
An	5	11	9	3	31	21	3	31	2	4	33	23	2
Ab	55	62	57	50	68	74	49	63	61	59	64	71	61
Or	40	27	34	47	2	5	48	6	37	37	3	6	37

TABLE 2
(continued)

	Outer Rind Dike				
Rock	Pl-rich quartz syenite	Perthite qtz syenite		PA granite	
Sample #	IL-167	IL-147		IL-157	IL-125
Analysis	40	41	42	43	44
Feldspar	Afs	Afs phenocryst, vein perthite (scanning)			
	Matrix			n=2	n=3
SiO_2	64.67	65.65	65.45	66.86	67.25
Al_2O_3	18.66	18.83	19.17	18.85	18.80
FeO*	0.42	0.54	0.49	0.20	0.33
CaO	0.09	0.15	0.36	0.12	0.14
Na_2O	1.59	5.33	5.42	6.35	6.73
K_2O	14.16	8.99	8.70	8.12	7.10
BaO	n.d.	0.11	0.29	-	n.d.
Total	99.58	99.60	99.88	100.49	100.35
Atoms to 8 oxygens					
Si	2.985	2.977	2.965	3.003	3.002
Al	1.015	1.007	1.024	0.997	0.989
Fe	0.016	0.020	0.019	0.008	0.012
Ca	0.004	0.007	0.017	0.006	0.006
Na	0.142	0.469	0.476	0.553	0.582
K	0.834	0.520	0.503	0.465	0.405
Ba	n.d.	0.002	0.005	n.d.	n.d.
End members, mol.%					
An	0	1	2	1	1
Ab	14	47	48	54	59
Or	85	52	51	45	41

(1) The analyses are selected points or scanned areas (in perthites). (2) FeO* = Fe total as FeO. (3) n.d.=not determined; "-", below the detection limit. (4) Abbreviations: Afs, alkali feldspar; Pl, plagioclase; TFS, ternary feldspar; Alk, alkaline; PA, peralkaline. (5) Core and rim with the same number = core and rim from a single phenocryst. (6) Samples marked with superscript "*" = ternary feldspars used as mineral thermometers.

Wadi Shagar Musa intrusion. It is a light gray, porphyritic rock, with medium grained phenocrysts of perthite, quartz, riebeckite and aegirine. Perthite (10-20%) with compositions of Ab_{51-56} Or_{43-49} (table 2, samples 3, 5) is prismatic, with corroded borders. Quartz (5-10%) is anhedral, mostly corroded. Mafic minerals are pure riebeckite (1.5-6%) and aegirine (0-1%) (tables 3 and 4; fig. 4A). Riebeckite phenocrysts are subhedral to euhedral, frequently with abundant poikilitic quartz and feldspar crystals from the matrix. Aegirine is observed in a few samples, commonly forming anhedral spongy crystals (0.5-2.5 mm) and smaller crystals without poikilitic inclusions. Textural relationships suggest that riebeckite and aegirine crystallized together. The microcrystalline to fine grained matrix constitutes 60 to 70 percent of the rock volume. It consists of the same mineral assemblage, which forms the phenocrysts. Alkali feldspar in the matrix contains less albite molecules (Ab_{33-38} Or_{62-64}) than the alkali feldspar phenocrysts (table 2, samples 4, 6). Accessories are opaque minerals, zircon, apatite and sphene. Matrix is microgranitic.

Riebeckite–arfvedsonite two-feldspar (albite and alkali feldspar) porphyritic microgranite comprises the lower part of the Wadi Shagar Musa body and the necks of Gebel Musa and Gebel Abu Rumeil. It is a red to pink colored porphyritic rock, very similar in mineral composition to the riebeckite-perthite porphyritic microgranite described

TABLE 3

Chemical compositions of amphiboles in main rock types of ring dikes and ignimbrites from the Katherina Ring Complex (microprobe analysis, wt.%)

	Wadi Shagar Musa		G. Musa	Inner Ring Dike			Outer Ring Dike	
Rock	PA microgranite			Pl-rich quartz syenite			PA granophyre	
Sample #	AG-55	AG-150	AG-57	AG-2	AG-158		AG-9	
Grain #	1	2	3	4	5	6	7	8
SiO_2	50.58	48.56	48.46	46.07	45.06	46.39	46.66	49.38
TiO_2	0.47	1.3	1.35	1.19	1.36	1.33	1.1	0.54
Al_2O_3	2.29	2.45	1.31	6.25	6.71	6.19	3.55	2.35
FeO	31.82	33.44	33.25	21.6	21.12	20.34	28.39	24.9
MnO	0.93	1.53	1.82	0.98	1.04	1.1	1.36	1.3
MgO	1.68	0.91	0.46	8.93	9.74	10.11	4.68	7.46
CaO	0.72	1.87	0.59	10.85	10.55	10.46	7.97	7.92
Na_2O	6.79	6.16	8.23	1.52	1.78	1.51	3.22	3.09
K_2O	1.29	1.24	1.34	0.78	0.95	0.74	1.13	0.98
F	1.32	1.06	1.72	n.d	n.d	n.d	n.d	n.d
Cl	-	-	-	n.d	n.d	n.d	n.d	n.d
	97.89	98.52	98.53	98.17	98.31	98.17	98.06	97.92
O=F, Cl	0.56	0.45	0.72					
Total	97.33	98.07	97.81	98.17	98.31	98.17	98.06	97.92
Atoms to 23 oxygens and 13 cations in (T + C) sites								
Si^{iv}	7.872	7.602	7.772	6.921	6.729	6.877	7.261	7.499
Al^{iv}	0.128	0.398	0.228	1.079	1.18	1.081	0.651	0.42
T-Fe^{3+}					0.091	0.042	0.088	0.08
Al^{vi}	0.291	0.054	0.02	0.027				
Fe^{3+}	1.182	1.293	0.845	0.698	0.892	0.93	0.628	0.7
Ti	0.055	0.153	0.163	0.134	0.153	0.148	0.129	0.062
Mg	0.39	0.212	0.11	2	2.168	2.234	1.086	1.689
Fe^{2+}	2.959	3.085	3.615	2.016	1.655	1.55	2.978	2.382
Mn	0.123	0.203	0.247	0.125	0.132	0.138	0.179	0.167
Ca_B	0.12	0.314	0.101	1.746	1.688	1.661	1.329	1.289
Na_B	1.88	1.686	1.899	0.254	0.312	0.339	0.671	0.711
Na_A	0.169	0.184	0.661	0.189	0.204	0.095	0.3	0.199
K_A	0.256	0.248	0.274	0.149	0.181	0.14	0.224	0.19
Sum A	0.425	0.431	0.935	0.339	0.385	0.235	0.525	0.389

above. The main distinctions are the presence in the matrix of subhedral and euhedral albite crystals, up to 11 percent (fig. 3B), as well as annite-enriched biotite flakes (table 5), and arfvedsonite in some of the samples.

Quartz monzonite and Pl-rich quartz syenite.—These rocks are described as a single mapping unit because they cannot be distinguished in the outcrops. Below, this rock

TABLE 3
(continued)

	Outer Ring Dike										
Rock	Qtz monzonite - Pl-rich quartz syenite					Afs qtz syenite		Afs granite			
Sample #	IL-74		IL-145			IL-69		IL-147		IL-157	
	9	10	11	12	13	14	15	16	17	18	19
SiO_2	47.61	47.84	45.49	46.59	52.11	46.62	45.85	45.68	49.64	44.04	45.1
TiO_2	0.95	0.67	1.4	0.99	0.12	1.2	0.88	1.31	0.4	1.27	1.28
Al_2O_3	4.71	4.66	5.7	4.51	1.1	5.56	5.67	5.21	3.24	4.85	4.93
FeO	20.28	19.84	24.97	23.79	22.38	15.01	18.48	25.72	22.31	28.55	27.96
MnO	1.01	1.02	1.32	1.46	1.26	0.68	0.96	1.71	1.34	1.83	1.54
MgO	10.94	11.51	7.4	8.38	9.83	14.15	10.62	6.92	9.34	5.11	5.23
CaO	9.78	9.87	9.6	9.81	11.19	10.93	11.03	9.43	11.07	9.21	9.49
Na_2O	1.5	1.53	1.86	1.53	0.25	1.88	1.55	1.98	1.01	1.86	2.2
K_2O	0.51	0.44	0.68	0.54	0.14	0.93	0.74	0.71	0.44	0.81	0.73
F	0.52	0.52	0.98	1.2	0.55	0.89	n.d	1.18	0.87	0.8	1.43
Cl	0.22	0.1	0.14	-	-	0.06	n.d	0.15	0.09	0.05	0.11
	98.03	98	99.54	98.8	98.93	97.91	95.78	100	99.75	98.38	100
O=F, Cl	0.27	0.24	0.44	0.51	0.23	0.39		0.53	0.39	0.35	0.63
Total	97.76	97.76	99.1	98.29	98.7	97.52	95.78	99.47	99.36	98.03	99.37
Atoms to 23 oxygens and 13 cations in (T + C) sites											
Si^{iv}	7.034	7.032	6.853	7.021	7.704	6.864	6.989	6.899	7.377	6.836	6.951
Al^{iv}	0.819	0.807	1.011	0.8	0.192	0.964	1.011	0.927	0.567	0.887	0.895
T-Fe^{3+}	0.147	0.162	0.135	0.179	0.105	0.172		0.174	0.056	0.277	0.155
Al^{vi}							0.006				
Fe^{3+}	1.133	1.193	1.056	1.036	0.626	0.71	0.599	1.035	0.633	1.084	0.818
Ti	0.106	0.074	0.159	0.112	0.013	0.133	0.101	0.149	0.045	0.148	0.148
Mg	2.409	2.522	1.662	1.882	2.166	3.106	2.413	1.558	2.069	1.182	1.202
Fe^{2+}	1.225	1.084	1.955	1.782	2.036	0.966	1.757	2.04	2.084	2.345	2.631
Mn	0.126	0.127	0.168	0.186	0.158	0.085	0.124	0.219	0.169	0.241	0.201
Ca_B	1.548	1.554	1.55	1.584	1.772	1.724	1.801	1.526	1.763	1.532	1.567
Na_B	0.43	0.436	0.45	0.416	0.072	0.276	0.199	0.474	0.237	0.468	0.433
Na_A	0	0	0.093	0.031	0	0.261	0.259	0.106	0.054	0.092	0.224
K_A	0.096	0.083	0.131	0.104	0.026	0.175	0.144	0.137	0.083	0.16	0.144
Sum A	0.096	0.083	0.224	0.135	0.026	0.436	0.403	0.243	0.137	0.252	0.368

Sodic amphiboles: 1–3 = riebeckite. Sodic-calcic amphiboles: 7 and 8 = katophorite. Calcic amphiboles: 4–6, 9, 10, 13–15 = magnesio-hornblende; 11, 12, 16–19 = ferro-hornblende. Nomenclature after Leake (1978). n.d. = no data. "-"= below detection limit.

type is called for brevity quartz monzonite-syenite. The quartz monzonite-syenite forms the Gebel Abbas Pasha body and makes up the dominant parts of the IRD and ORD (fig. 1). In all bodies the compositions straddle the borderline between quartz monzonite and quartz syenite (fig. 3A). The rocks are dark red to dark gray, porphyritic, with various phenocrysts of about 3 to 6 mm and fine grained matrix. The

TABLE 4

Microprobe analyses of pyroxenes in representative rock types of ring dikes from the Katherina Ring Complex (wt%)

	Wadi Shagar Musa				Inner Ring Dike		Outer Ring Dike		
Rock	Peralkaline microgranite				Pl-rich quartz syenite porphyry				
Sample #	AG-150		AG-57		AG-158			IL-69	IL-167
Grain #	1	2	3	4	5	6	7	8	9
SiO_2	52.39	51.13	50.92	50.68	54.11	53.17	53.69	50.94	51.24
TiO_2	0.39	0.16	0.31	0.37	0.20	0.11	0.27	0.70	0.73
Al_2O_3	0.86	0.45	0.33	0.80	1.44	0.83	1.69	1.94	2.42
FeO*	30.94	31.91	30.74	30.60	19.07	23.81	19.95	10.02	9.80
MnO	0.07	0.13	0.51	0.56	1.63	2.37	1.67	0.83	0.86
MgO	0	0	0	0	16.63	15.92	16.78	14.49	13.71
CaO	0.13	0.91	2.45	3.02	5.36	1.8	4.34	19.63	19.93
Na_2O	13.3	12.56	12.17	11.48	0.38	0.24	0.48	0.57	0.77
K_2O	0	0	0	0	0.09	0	0.11	0	0.06
Total	98.08	97.25	97.43	97.51	98.91	98.25	98.98	99.12	99.52
Atoms to 6 oxygens and 4 cations									
Si	1.985	1.968	1.96	1.959	2.068	2.079	2.051	1.912	1.917
Al iv	0.015	0.02	0.015	0.036				0.086	0.083
Fe^{3+}iv		0.011	0.025	0.004				0.002	
Al vi	0.024				0.065	0.038	0.076		0.023
Ti	0.011	0.005	0.009	0.011	0.006	0.003	0.008	0.02	0.021
Fe^{3+}	0.946	0.96	0.93	0.88				0.09	0.077
Fe^{2+}	0.034	0.056	0.035	0.106	0.609	0.609	0.637	0.223	0.229
Mn	0.002	0.004	0.017	0.018	0.053	0.079	0.054	0.026	0.027
Mg					0.947	0.958	0.916	0.811	0.765
Ca	0.005	0.038	0.101	0.125	0.219	0.075	0.178	0.789	0.799
Na	0.977	0.938	0.908	0.861	0.028	0.018	0.036	0.041	0.056
K					0.004		0.005		0.003

5 & 6 = large crystals; 7–9 = small phenocrysts.

phenocrysts constitute about 60 to 75 percent of the rock volume. One specific feature of this rock type is the large scatter of modal composition (table 1; Online table 1-SD, http://earth.geology.yale.edu/~ajs/SupplementaryData/2013/04EyalSD-1.doc): perthite, 33 to 55 percent; plagioclase, 24 to 40 percent; quartz, 5 to 13 percent; mafic minerals (Am, Cpx, Bi), 6 to 16 percent; opaque mineral, 2 to 7 percent. One more distinctive feature is the evidence of extensive corrosion of phenocrysts, mainly plagioclase, by the host melt and reaction rims found around plagioclase crystals. This feature is illustrated below and discussed in the second half of the paper.

Perthite phenocrysts are anhedral, sized from 1 to 5 mm, with fine veined to coarse patchy texture. Frequently they are overgrown with a perthitic rim, 0.2 to 1.0 mm wide, in which the albite lamellae are in the same orientation as that in the center

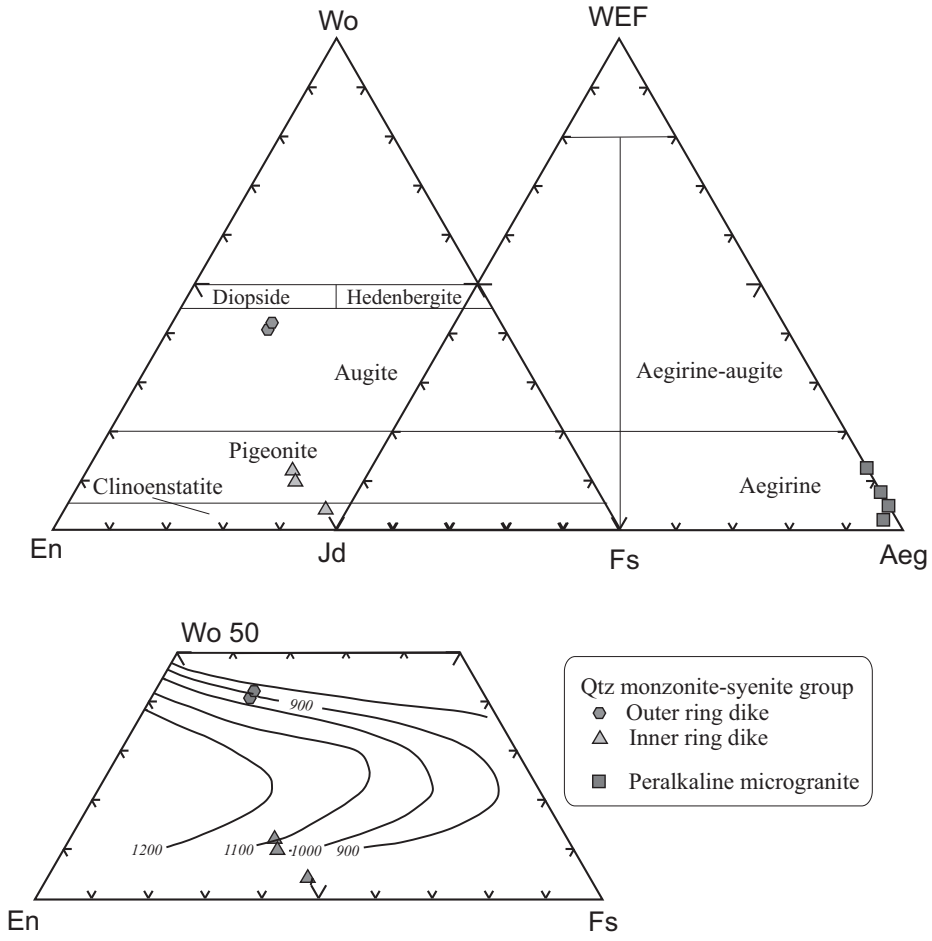

Fig. 4. (A) Pyroxene compositions plotted in the En-Wo-Fs and Jd-WEF-Aeg classification diagrams (after Morimoto and others, 1988). (B) Estimation of temperature of pyroxene crystallization at $P < 2$ kbar (after Lindsley, 1983).

of the crystal. Most phenocrysts (core and rim) and crystals in the matrix are characterized by noticeable predominance of albite over orthoclase: $An_{0\text{-}4}$ $Ab_{51\text{-}70}$ $Or_{30\text{-}50}$ (fig. 5; table 2).

Plagioclase phenocrysts occur in two generations, Pl-1 ($An_{28\text{-}35}$) and Pl-2 ($An_{20\text{-}24}$); they are commonly unzoned and rimmed with perthite. Polysynthetic twinning is characteristic of least corroded euhedral and subhedral crystals. In places the newly formed alkali feldspar rims, along with fine-grained matrix, split a single prismatic plagioclase grain into a cluster of shapeless and rounded fragments (figs. 6A-6C). Some feldspar phenocrysts have a texture similar to patch perthite and antiperthite. However, the plagioclase phase composition in these phenocrysts is $An_{30\text{-}33}$ and $An_{21\text{-}24}$, which is characteristic of Pl-1 and Pl-2, respectively, whereas the alkali feldspar contains 30 percent albite (figs. 6D and 6E). Moreover, an intermediate reaction product corresponding to ternary feldspar is found in several thin sections (for example, figs. 5 and 6E). It is pertinent to note that even the least altered plagioclase

TABLE 5

Microprobe analyses of biotite in representative rock types of ring dikes from the Katherina Ring Complex (wt%)

	G. Musa	Inner Ring Dyke		Outer Ring Dyke				
Rock	PA granite	Qtz syenite		Granophyre	Qtz monzonite - syenite			
Sample #	AG-57	IL-158		AG-9	IL-167		IL-74	
SiO_2	45.59	36.70	37.55	38.78	38.16	38.35	36.84	36.99
TiO_2	5.18	2.25	3.56	2.94	3.16	3.14	4.24	4.10
Al_2O_3	11.32	12.33	11.78	9.29	13.59	12.38	11.94	11.26
FeO	19.23	22.38	24.29	27.29	16.54	16.41	23.65	24.89
MnO	1.41	0.41	0.43	0.67	0.14	0.44	0.43	0.29
MgO	0.29	13.09	10.74	7.73	14.19	15.15	9.91	9.57
CaO	0.51	0.04	0.15	0.24	0.13	0.05	0.07	-
Na_2O	1.20	0.09	0.10	0.11	0.48	0.07	0.17	0.14
K_2O	8.94	8.00	8.43	9.13	9.79	9.19	8.62	8.84
BaO	0.45	n.d	n.d	n.d	-	0.21	0.11	0.20
F	1.31	n.d	n.d	n.d	0.71	0.94	0.69	0.76
Cl	-	n.d	n.d	n.d	0.11	0.19	0.31	0.27
	95.45	95.30	97.02	96.17	96.99	96.53	96.98	97.31
O=F, Cl	0.55				0.33	0.45	0.37	0.39
Total	94.90	95.30	97.02	96.17	96.66	96.08	96.61	96.92
Atoms to 11 oxygens								
Si	3.476	2.835	2.877	3.058	2.855	2.889	2.856	2.881
Al iv	0.524	1.123	1.063	0.863	1.145	1.098	1.091	1.034
Ti iv		0.042	0.060	0.079		0.013	0.053	0.085
Al iv	0.493				0.053			
Ti vi	0.297	0.09	0.15	0.10	0.178	0.17	0.19	0.16
Fe	1.226	1.446	1.556	1.800	1.035	1.033	1.534	1.621
Mn	0.091	0.027	0.028	0.044	0.009	0.028	0.028	0.019
Mg	0.033	1.508	1.227	0.909	1.582	1.701	1.146	1.111
Ca	0.042	0.003	0.012	0.020	0.011	0.004	0.006	
Na	0.178	0.014	0.015	0.016	0.069	0.010	0.025	0.021
K	0.870	0.789	0.824	0.918	0.935	0.883	0.852	0.878
Ba	0.013					0.006	0.003	0.006
F	0.317				0.169	0.224	0.169	0.188
Cl					0.013	0.025	0.040	0.036

crystals contain 3 to 5 percent of Or molecule and 0.25 to 0.77 weight percent BaO; the latter is comparable with the barium content in the alkali feldspars (table 2).

Ternary feldspar (Smith and Brown, 1988) exhibits a wide variety of forms: (a) subhedral phenocrysts, part of them zoned; (b) small crystals in the matrix, and cores which are rimmed with perthite (fig. 6F; table 2, for example analyses 10 and 11, 26 and 27, respectively); (c) rims around plagioclase and rarely around alkali feldspar; and (d) as thin veins within the plagioclase crystals. The presence of ternary feldspar phenocrysts, both zoned and rimmed with perthite, suggests crystallization of this mineral from magma. Part of the ternary feldspar was produced as a result of reaction between the feldspar phenocrysts and the host melt (see also fig. 6E). In the Ab-An-Or

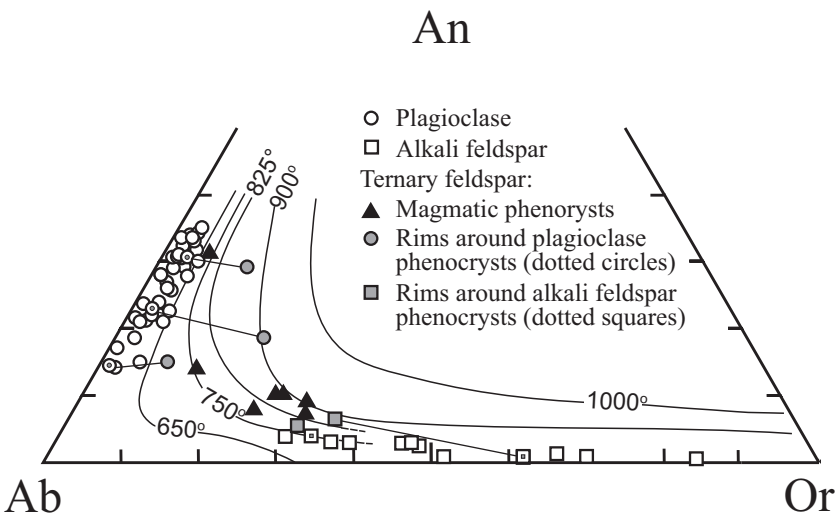

Fig. 5. Compositions of plagioclase, alkali feldspar and ternary feldspar from the ring dike rocks of the Katherina Ring Complex on the Ab–An–Or diagram with solvus isotherms at P = 2 kbar for ternary feldspars (after Lindsley and Nekvasile, 1989; Nekvasile, 1992).

diagram (fig. 5) we plot ternary feldspars crystallized from magma and those produced by reaction. Most of magmatic ternary feldspars form a cluster with a compositional range of $An_{7\text{-}15}$ $Ab_{55\text{-}65}$ $Or_{35\text{-}42}$.

Amphiboles (table 3) are the main mafic phenocrysts, 5 to 12 percent. In chemical composition they are classified, after Leake (1978), as magnesio-hornblende; a few grains are ferro-hornblende. Amphiboles contain a noticeable amount of F (0.5-1.2 wt.%) and Cl (about 0.1 wt.%). Pyroxene, 0 to 2.5 percent, forms prismatic and tabular phenocrysts about 1 to 2 mm in length. According to chemical compositions (table 4), augite and pigeonite are recognized (fig. 4). Frequently pyroxene is partially replaced or rimmed by magnesio-hornblende. Both larger and smaller pyroxene crystals are found as inclusions in the plagioclase phenocrysts. Such interrelations suggest that pyroxene is one of the liquidus minerals.

The matrix of the quartz monzonite-syenite is granitic and quartz syenitic, fine to medium grained, consisting mainly of alkali feldspar and quartz, with secondary small prismatic elongated crystals of plagioclase ($An_{14\text{-}16}$), tiny biotite flakes, tabular amphibole and subhedral Fe-Ti oxide grains. Biotite contains noticeable proportions of phlogopite and annite, 0.7 to 0.9 weight percent F and 0.1 to 0.3 weight percent Cl (table 5).

Quartz syenite.—This rock type is closely associated with the quartz monzonite-syenite group and also makes up separate dikes. It is a dark reddish brown porphyritic rock with dominating phenocrysts (up to 70-85%) and a microgranite matrix. It is distinguished from the rocks of the above group by its lower content of plagioclase, 10 to 17 percent (fig. 3A; table 2), commonly $An_{20\text{-}24}$, and a slightly smaller amount of mafic minerals in most samples. Perthite constitutes 50 to 75 percent of the phenocrysts. The amount of quartz varies widely, from 5 to 18 percent (table 1). Mafic minerals are mostly hornblende (2-9.5%) with secondary biotite (0.5-4%) and in places clinopyroxene, about 1 percent. Mafic minerals are of the same composition as those in the quartz monzonite-syenite group. The fine grained matrix is composed of interstitial granophyric and microgranitic quartz–Afs aggregate, anhedral to subhedral

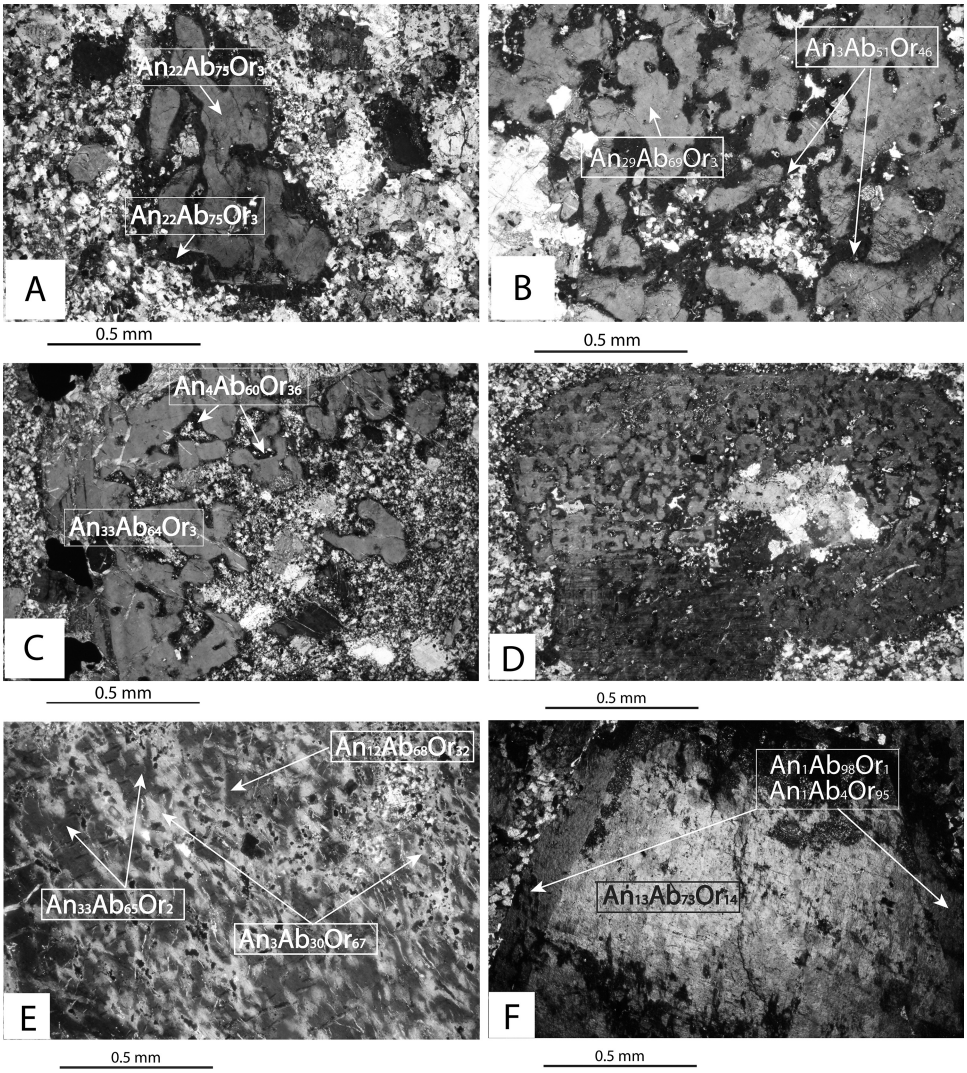

Fig. 6. Microphotographs illustrating reactions of plagioclase crystals with the host silicic melt (microgranite matrix). (A-C) Resorbed plagioclase crystals (gray) with alkali feldspar reaction rims (dark), samples AG-2 (A and B) and IL-167 (C). (D) and (E), bulk replacement of plagioclase (An_{33}) by alkali feldspar, which resulted in formation of a texture resembling patch perthite; sample AG-2. As shown in figure E, an intermediate product of reaction is ternary feldspar An_{12} Ab_{66} Or_{32}. (F) Crystal of magmatic ternary feldspar (light) overgrown with a perthite rim (dark gray), sample IL-88.

plagioclase $An_{8\text{-}14}$, 5 to 7 percent, mafic (hornblende, Fe-Ti oxide, biotite) and accessory minerals. In the ORD several patches of granite with 20 to 27 percent quartz are found within the quartz syenite outcrops (fig. 3A; table 1 and Online table 1-SD, http://earth.geology.yale.edu/~ajs/SupplementaryData/2013/04EyalSD-1.doc).

Kataphorite microgranite body in the IRD (fig. 2).—The microgranite is a reddish light gray porphyritic rock composed mainly of medium grained, anhedral and subhedral perthite phenocrysts with fine-veined to patchy texture and outer perthitic rims. Quartz is subhedral, with outer rings of inclusions. The matrix (about 25%) is

microgranitic, in places granophyric. Mafic minerals in the matrix are small crystals of kataphorite (table 3, samples 7, 8) and flakes of biotite enriched in the annite molecule (table 5, sample AG-9). Accessories are sphene, apatite, and zircon.

Perthite quartz syenite and granite from the ORD.—Perthite quartz syenite is a reddish brown rock that appears in two varieties: medium or coarse grained inequigranular and porphyritic. It consists of red subhedral perthite crystals (72-79%); anhedral quartz (9-17%); euhedral plagioclase (3-6.4%) surrounded with a perthitic rim; 2 to 5.7 percent of ferro-hornblende (table 3, samples 16 and 17), biotite (0.5-2%), ore mineral (1-4.5%) and accessories. In the porphyritic varieties the fine grained matrix amounts to 45 percent and consists of 20 percent perthite, 10 percent quartz, 10 percent plagioclase and 5 to 10 percent mafic minerals. In some areas the amount of quartz exceeds 20 percent, and the perthite quartz syenite gradually changes to perthite granite.

Granites of the Katherina pluton.—These rocks are represented by syenogranite, two-feldspar (Ab-Afs) and perthite granite (for more details see Katzir and others, 2007).

Syenogranite is a grayish pink rock with grain size 5 to 10 mm and subhedral texture. The average contents of alkali feldspar, quartz and plagioclase are 46, 30 and 22 volume percent, respectively. Plagioclase forms prismatic crystals $An_{7\text{-}11}$, which are commonly zoned ($An_{15\text{-}20}$ in the core). Perthite crystals are anhedral, and quartz is observed as rounded and anhedral grains. Minor brown biotite, intermediate between annite and phlogopite, with 1.6 to 3.5 weight percent F occurs as euhedral flakes. Accessories are titanomagnetite, titanite, fluorite, zircon and apatite.

Perthite granite is distinguished from the syenogranite by its red color, smaller grain size (3-6 mm), absence of plagioclase crystals and predominance of anhedral and graphic texture. It consists of equant perthite (~65%) and quartz grains (32%), with flakes of light brown biotite. Almost all perthite crystals are dense brown turbid patch perthites. The amount of accessory fluorite in the perthite granite is noticeably higher.

Ab-Afs granite is mainly characterized by presence of almost pure albite prismatic crystals ($An_{1\text{-}3}$, rarely $An_{5\text{-}7}$), ranging from 4 to 20 percent. Anhedral perthite (41-65%) is similar to those in perthite granite. In places, rare zoned plagioclase grains are also present. According to the IUGS classification (Le Maitre, 1989), both perthite granite and Ab-Afs granite are referred to as alkali-feldspar granite.

GEOCHEMISTRY

Major and trace element compositions were determined for 53 samples, of which 34 had complete analyses of REE. The results are presented in Appendix table 4-SD and further illustrated in figures 7, 8 and 9. The data for the 33 most representative samples are reported in table 6. The chemical data for three rhyolite ignimbrite samples are included in the table, but not used in the graphic presentations because their chemical compositions vary widely possibly due to admixture of small rock fragments during eruption.

According to the classification of Streckeisen and Le Maitre (1979), the volcanic, subvolcanic and plutonic rocks forming the KRC fall into three rock types: (a) alkali feldspar granite and rhyolite; (b) alkali feldspar quartz syenite; and (c) quartz syenite (fig. 7A). The latter rock type also comprises the quartz monzonite—Pl-rich quartz syenite group that dominates the ring dikes and makes up the Abbas Pasha subvolcanic intrusion. All samples of this group also plot in the "syenite" field in the TAS classification diagram (SiO_2 vs. Na_2O+K_2O, not shown). This is the only group corresponding to the calc-alkaline granitoid field in the classification diagram of SiO_2 vs. $(Na_2O+K_2O)/Al_2O_3$ (fig. 7B, after Liégeous and Black, 1987). The enhanced K_2O (4.8-5.5 wt.%) and the range of SiO_2 (61-65 wt.%) suggest that they belong to the shoshonitic series (after Rickwood, 1989). All the rest of the KRC rocks are alkaline

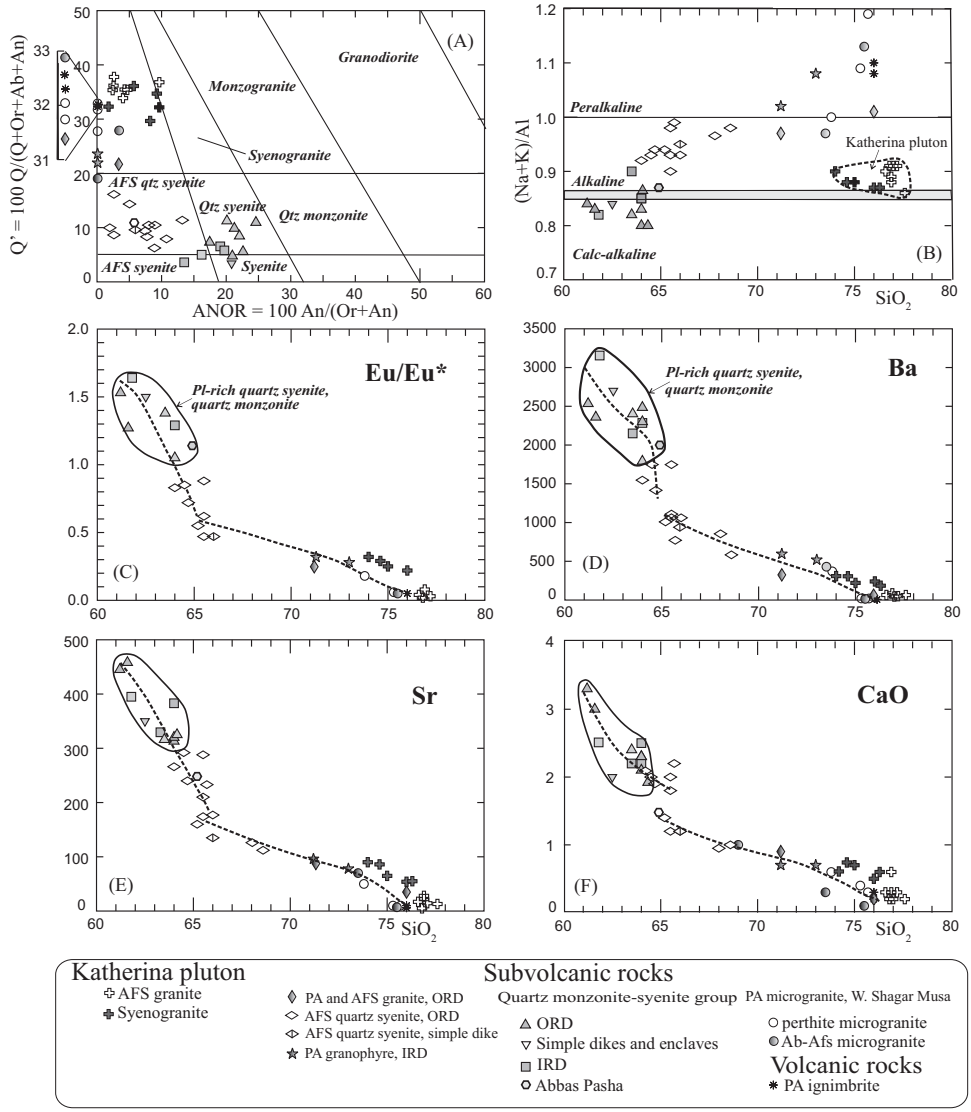

Fig. 7. Classification and bivariate diagrams for igneous rocks of the KRC. (A) Main rock type compositions in the diagram 100An/(Or+An) vs. 100 Q/(Q+Or+Ab+An), after Streckeisen and Le Maitre (1979). (B) Compositions of igneous rocks in the classification diagram SiO_2 vs. $(Na_20+K_2O)/Al_2O_3$ (agpaitic index, mol.%), after Liégeois and Black (1987). (C-F) Silica variation diagrams demonstrating trends of compositional changes of igneous rocks.

and peralkaline granites (figs. 7A and 7B). The agpaitic indices of the highly alkaline subvolcanic rocks and volcanic peralkaline ignimbrite show a positive correlation with silica content, whereas the data points of granites from the Katherina pluton form a separate cluster in the plot (fig. 7B).

In the silica variation diagrams (figs. 7C-7F) all data points of subvolcanic and volcanic rocks are arranged along two curves, one is steeply dipping and the other slopes gently. The curves meet in the alkali feldspar (AFS) quartz syenite compositions with about 65 percent SiO_2. The steeply dipping curves in the plots characterize the

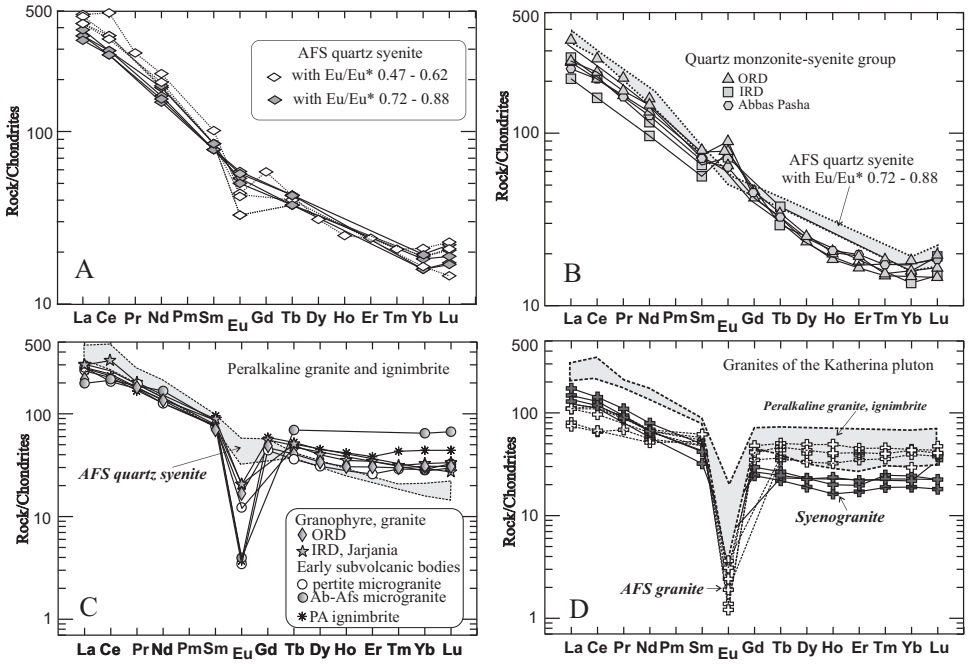

Fig. 8. Chondrite normalized REE patterns of the KRC. (A) Alkali feldspar quartz syenite. (B) Quartz monzonite–syenite group, ring dikes. (C) Peralkaline granites and volcanic ignimbrites. (D) Syenogranite and perthite granite from the Katherina pluton. Chondrite values from Sun and McDonough (1989).

systematic compositional change in the lower silica rock types (61-65 wt.% SiO_2), the quartz monzonite—quartz syenite group and part of the AFS quartz syenite. The specific feature of these rocks is enhanced Eu/Eu* ratios. In the quartz monzonite–syenite group the ratios vary from 1.63 to 1.05 (see also fig. 8B). In the AFS quartz syenite they vary from 0.83 to 0.88 to 0.47. The more evolved AFS quartz syenite varieties with low Eu/Eu* values are located near the intersection of the two curves (figs. 7C and 8A). The enhanced Eu/Eu* values in the quartz monzonite-syenite group suggest that at least part of the highly corroded plagioclase and pyroxene crystals in these rocks are accumulated crystals or xenocrysts [henceforth we use the term "accumulated crystals" defined by Kelemen and others (2007) as "crystals that are in excess in the amount that could crystallize from a melt in a closed system"]. In the plagioclase-absent AFS quartz syenite with Eu/Eu* attaining 0.83 to 0.88 the crystals that likely provided higher contents of Eu and Ba are accumulated alkali feldspars (figs. 7C, 7D and 8A). However, in the quartz monzonite-syenite group systematic increase in Ba with decreasing silica (up to 3000 ppm; fig. 7D) does not necessarily indicate accumulation of alkali feldspar crystals because plagioclase in these rocks also contains 0.25 to 0.77 weight percent Ba (table 2).

The steep decrease of Eu/Eu* from 1.63 to 0.47 and simultaneous increase of SiO_2 in quartz monzonite-syenite and AFS quartz syenite can be interpreted as evidence of a systematic decrease in accumulated crystals (or xenocrysts) in these granitoid rocks. Note that the decrease of Eu/Eu* is accompanied by a parallel decrease in Ba, Sr, CaO (figs. 7C-7F), as well as MgO and FeO^T (not shown). The REE patterns (fig. 8B) show enrichment of LREE in the AFS quartz syenite as compared with the quartz monzonite-syenite.

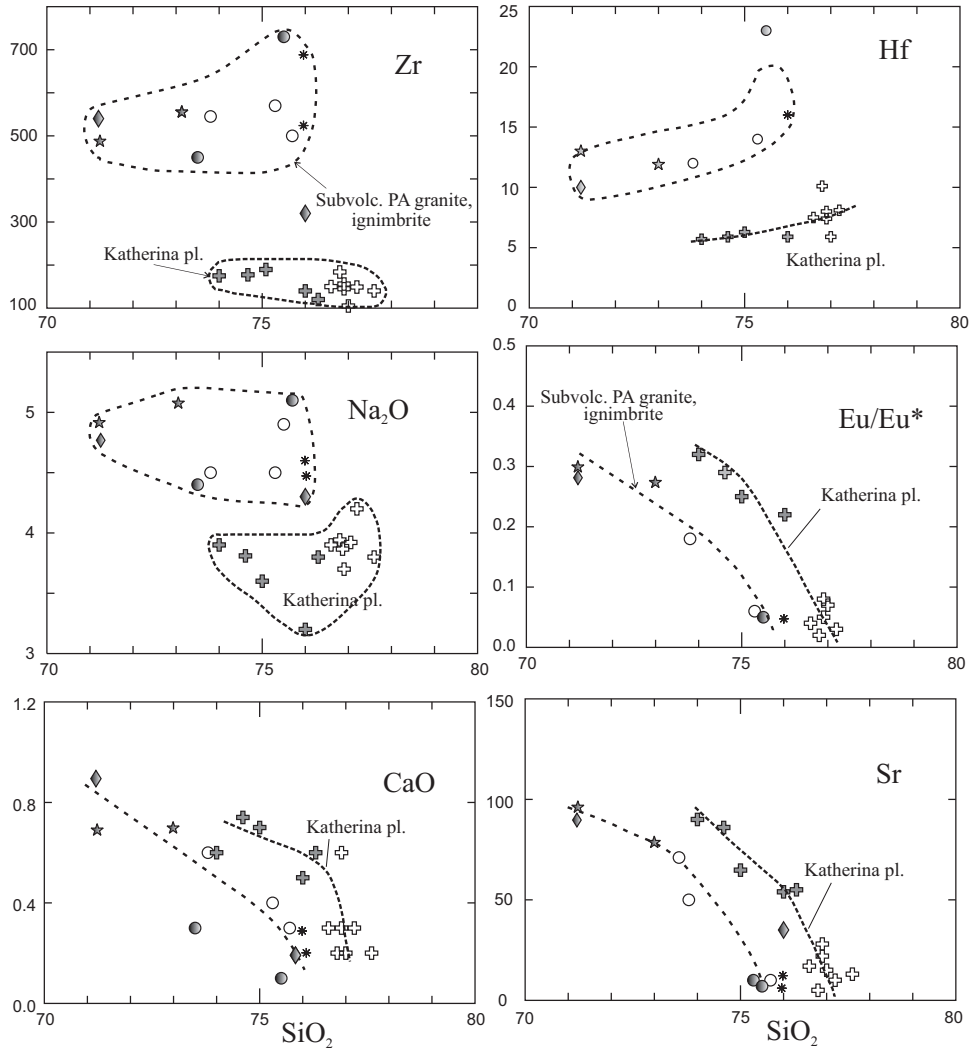

Fig. 9. Silica variation diagrams showing regular distinctions between the granites of the Katherina pluton and the earlier peralkaline highly silicic subvolcanic rocks and ignimbrite with $SiO_2 > 70$ wt.%. Symbols as in figure 7.

The gently sloping curves demonstrate a systematic change of chemical compositions from the evolved AFS quartz syenite to perthite alkaline and porphyritic peralkaline granite and peralkaline ignimbrite (figs. 7C-7F): decrease of Sr, Ba, Eu/Eu*, CaO, as well as MgO, FeO^T, Zr, and Nb (not shown) with increase of SiO_2 from 65 to 76 weight percent. This trend is similar to the liquid line of descent. The compositions of granite varieties from the Katherina pluton also approach the trend lines.

A comparison of Eu/Eu* ratios and REE patterns in the AFS quartz syenite and the most evolved rocks, peralkaline granite and ignimbrite (figs. 7C and 8C), shows that the latter silica rich peralkaline rocks are characterized by the lowest Eu/Eu* values, down to 0.04 to 0.18, and highest HREE (table 6).

TABLE 6

Chemical compositions of representative igneous rocks from the Katherina Ring Complex

Unit	*Volcanic rocks*					*Wadi Shagar Mussa* Upper part	Lower part		*G. Musa*
Rock type	Rhyolitic ignimbtite		PA rhyol. ignimbrite		Glass	Riebeckite perthite granite		Riebeckite granite	Ab-Afs
Sample #	AG-178	AG-202	AG-41		AG-41^{MP}	AG-139	AG32	AG-77	AG-57
Analysis	1	2	3	4	5	6	7	8	9
SiO_2	72.50	69.20	76.00	76.00	78.14	73.80	75.30	73.50	75.50
TiO_2	0.32	0.49	0.13	0.14	-	0.23	0.12	0.33	0.13
Al_2O_3	14.50	14.80	11.50	11.50	11.66	12.60	11.50	12.80	11.50
Fe_2O_3	1.33	1.45	2.10	1.92		2.10	2.39	2.64	1.82
FeO	0.33	1.23	0.27	0.43	1.48	0.45	0.19	0.06	0.34
MnO	0.07	0.10	0.05	0.07	0.07	0.08	0.07	0.09	0.08
MgO	0.20	0.74	0.05	0.05	0.00	0.10	0.10	0.20	0.05
CaO	0.60	2.02	0.20	0.30	0.18	0.60	0.40	0.30	0.10
Na_2O	4.80	3.84	4.60	4.50	5.16	4.50	4.50	4.40	4.90
K_2O	4.40	4.36	4.70	4.60	3.84	4.80	4.70	4.80	4.60
P_2O_5	0.05	1.33	0.05	0.05		0.05	0.05	0.05	0.05
LOI	0.7	0.14	0.4	0.4		0.5	0.5	0.7	0.4
Total	99.80	99.70	100.05	99.96	100.53	99.81	99.77	99.86	99.47
NK/A	0.87	0.75	1.10	1.08	1.08	1.00	1.09	0.97	1.13
Rb	60	50	190	225		85	210	80	140
Ba	1150	1200	19	20		370	21	430	15
Sr	130	300	6	10		50	10	70	7
Zr	300	260	690	520		545	570	450	730
Nb	14	13	61			39	34.7		83
Y	37	25	71	66		48	39	47	79
Hf	7.0	7.3	16.0			12.0	14.0		23.0
Th	10.0	11.0	31.0			21.0	25.0		61.0
Ga			26.13				26.71		
Ta			7.78				7.22		
Sc	8.2	7.0	2.7			4.3	3.0		2.1
Pb	19	36	39	37		21	30	90	71
La	40	33	66			63	67		47
Ce	82	70	143			140	126		130
Pr			16.9				16.7		
Nd	42	33	64			60	59		78
Sm	9.10	6.10	13.22			12.00	11.59		13.00
Eu	2.30	1.30	0.22			0.71	0.20		0.23
Gd			12.14				9.05		
Tb	1.40	0.86	1.97			1.80	1.35		2.60
Dy			11.40				7.84		
Ho			2.36				1.58		
Er			6.34				4.29		
Tm			1.10				0.74		
Yb	4.20	3.10	7.50			4.80	4.88		11.00
Lu	0.70	0.51	1.12			0.77	0.83		1.70
*Eu/Eu**	0.76	0.65	0.05			0.18	0.06		0.05
$(La/Yb)_N$	6.3	7.0	5.8			8.7	9.0		2.8

Table 6
(continued)

Unit	*Abbas Pasha*	*Inner Ring Dike*		*Wadi Jarjaniya body*		*Outer Ring Dike*			
Rock type	Qtz monzonite - Pl-rich syenite			Katophorite Ab-Afs microgranite		Qtz monzonite - Pl-rich syenite			
Sample #	IL3AG	AG-148	AG-2	AG-9	AG-11	IL-167	IL-66	IL-74	IL-161
Analysis	10	11	12	13	14	15	16	17	18
SiO_2	64.90	63.50	64.00	71.20	73.00	64.00	61.20	61.60	64.00
TiO_2	0.72	0.76	0.78	0.30	0.30	0.82	1.06	0.98	0.80
Al_2O_3	16.90	17.40	17.50	13.30	13.00	17.00	17.00	17.10	16.20
Fe_2O_3	1.85	1.66	2.54	1.57	2.36	3.78	3.29	3.00	2.52
FeO	1.39	1.93	1.04	1.20	0.48	0.29	1.45	1.44	1.33
MnO	0.11	0.11	0.12	0.09	0.09	0.12	0.13	0.14	0.14
MgO	0.57	0.70	0.70	0.30	0.20	0.70	1.20	1.10	0.80
CaO	1.48	2.20	2.50	0.70	0.70	2.30	3.30	3.00	2.30
Na_2O	5.25	6.00	5.60	4.90	5.10	5.00	5.50	5.60	5.00
K_2O	5.67	5.30	5.20	5.10	5.20	4.90	4.80	4.60	4.90
P_2O_5	0.81	0.20	0.20	0.10	0.05	0.30	0.50	0.40	0.30
LOI	0.23	0.4	0.5	0.4	0.3	0.6	0.3	0.8	0.4
Total	99.88	100.16	100.68	99.16	100.78	99.81	99.73	99.76	98.69
NK/A	0.87	0.90	0.85	1.02	1.08	0.80	0.84	0.83	0.83
Rb	83	35	70	160	144	56	30	51	95
Ba	2000	2150	2285	595	519	2300	2534	2359	1790
Sr	240	325	383	96	78	320	445	458	325
Zr	320	300	300	540	563	310	251	327	354
Nb	22		21	43	50		16	22	22
Y	30	28	28	50	59	31	29	32	31
Hf	7.1		6.1	13.0	11.9		5.7	6.5	7.2
Th	12.0		9.5	22.0	21.0		6.8	6.9	10.5
Ga					33.90		23.50	25.70	23.94
Ta					5.77		2.48	2.58	3.69
Sc	6.9		9.0	4.8	4.4			9.1	
Pb		19	12	24	19		33	12	20
La	56		65	72	71		61	62	82
Ce	126		130	160	202		126	138	165
Pr	15.4				19.2		15.7	16.7	19.8
Nd	59		54	67	71		62	68	74
Sm	10.60		10.00	12.00	13.58		11.44	11.86	12.17
Eu	3.68		4.20	1.20	1.19		5.19	4.55	3.76
Gd	8.71				11.44		8.67	9.45	8.89
Tb	1.22		1.40	1.90	1.84		1.21	1.29	1.26
Dy	6.27				10.15		5.96	6.54	6.39
Ho	1.18				1.99		1.05	1.15	1.17
Er	3.28				5.71		2.74	3.20	3.00
Tm	0.44				0.80		0.38	0.39	0.47
Yb	2.98		2.70	5.00	5.58		2.51	2.70	3.10
Lu	0.47		0.49	0.69	0.85		0.37	0.42	0.50
*Eu/Eu**	1.14		1.29	0.30	0.28		1.53	1.27	1.05
$(La/Yb)_N$	12.5		15.9	9.5	8.4		16.0	15.1	17.6

TABLE 6
(continued)

Unit	*Outer Ring Dike*								
Rock type	Qtz monzonite - Pl-rich syenite	Perthite quartz syenite							PA granophyre
Sample #	IL-182	IL-68	IL-145	IL-67	IL-142	IL-88	IL-147	IL-84	IL-73
Analysis	19	20	21	22	23	24	25	26	27
SiO_2	63.50	64.00	65.50	64.70	64.50	65.20	65.50	65.50	71.20
TiO_2	0.81	0.75	0.78	0.73	0.80	0.62	0.66	0.62	0.31
Al_2O_3	17.20	16.20	15.80	16.00	16.60	16.00	15.70	15.70	13.80
Fe_2O_3	2.02	2.75	2.39	2.89	2.97	3.33	2.88	2.65	2.11
FeO	1.60	1.13	1.36	0.91	0.84	0.34	1.01	0.85	0.35
MnO	0.12	0.13	0.13	0.13	0.15	0.14	0.15	0.15	0.11
MgO	0.80	0.70	0.80	0.70	0.70	0.50	0.60	0.60	0.30
CaO	2.40	2.10	2.00	1.90	2.00	1.40	1.80	1.20	0.90
Na_2O	5.20	5.60	5.40	5.50	6.00	5.60	5.80	5.40	4.80
K_2O	5.10	5.20	4.90	5.50	5.20	5.40	5.40	5.30	5.10
P_2O_5	0.30	0.30	0.20	0.20	0.30	0.20	0.40	0.20	0.05
LOI	0.3	0.2	0.5	0.6	0.6	0.5	0.5	1.2	0.6
Total	99.35	99.05	99.76	99.76	100.66	99.22	100.40	99.37	99.63
NK/A	0.82	0.92	0.90	0.94	0.93	0.94	0.98	0.93	0.97
Rb	40	45	60	45	50	45	60	50	164
Ba	2402	1547	1747	1416	1748	1008	1085	1062	325
Sr	316	266	288	240	292	160	210	174	91
Zr	270	390	350	400	360	460	500	480	490
Nb	18	23	23	24	22		29	28	45
Y	25	30	31	32	30	33	32	33	56
Hf	5.9	8.7	8.2	8.0	7.4		8.1	11.0	10.0
Th	8.9	11.0	10.0	12.0	10.0		13.0	14.0	26.0
Ga									34.00
Ta									5.80
Sc	9.2	10.0	8.9	8.6	10.0	11.0	9.6	9.7	5.0
Pb	26	25	24	27	23	21	21	47	16
La	65	85	85	92	80	113	110	100	67
Ce	130	170	180	180	170	298	220	210	149
Pr						27.1			17.2
Nd	54	69	75	84	72	101	86	90	63
Sm	9.20	12.00	12.00	13.00	12.00	15.48	13.00	13.00	11.43
Eu	4.20	3.10	3.40	2.90	3.30	2.54	2.50	1.90	0.97
Gd						11.98			9.62
Tb	1.40	1.40	1.60	1.40	1.60	1.59	1.50	1.40	1.52
Dy						7.85			8.61
Ho						1.41			1.73
Er						3.98			5.03
Tm						0.53			0.76
Yb	2.10	2.70	2.70	3.10	3.30	3.57	2.80	3.20	5.25
Lu	0.35	0.44	0.43	0.48	0.56	0.58	0.37	0.53	0.78
*Eu/Eu**	1.38	0.83	0.88	0.72	0.85	0.55	0.62	0.47	0.28
$(La/Yb)_N$	20.4	20.8	20.8	19.6	16.0	20.9	25.9	20.6	8.5

TABLE 6
(continued)

Unit	Katherina pluton						
Rock type	Syenogranite			Ab-Afs granite		Perthite granite	
Sample #	D-163	D-165	D-82	D-54	D-93	D-43	D-40
Analysis	28	29	30	31	32	33	34
SiO_2	74	74.61	75	76.9	77	76.8	77.2
$Ti0_2$	0.2	0.18	0.17	0.07	0.07	0.07	0.07
Al_2O_3	13.2	13.23	12.9	12.1	12.4	12.1	12.4
Fe_2O_3	1.6	1.46	1.5	1.4	1.7	1.8	1.4
Fe0							
MnO	0.04	0.05	0.06	0.09	0.04	0.04	0.06
MgO	0.3	0.22	0.2	0.01	0.05	0.01	0.01
CaO	0.6	0.74	0.7	0.6	0.2	0.2	0.3
Na_2O	3.9	3.81	3.6	3.7	3.9	3.9	4.2
K_2O	5	4.95	5	4.2	4.5	4.3	4
P_20_5	0.05	0.48	0.05	0.05	0.05	0.05	0.05
LOI	0.5	0.07	0.3	0.6	0.3	0.3	0.5
Total	99.39	99.8	99.48	99.72	100.21	99.57	100.19
NK/A	0.9	0.88	0.88	0.88	0.91	0.91	0.91
Rb	216	243	243	394	373	384	335
Ba	309	307	221	36	45	42	50
Sr	90	86	64.8	22	15	5	10
Zr	175	176	184	156	105	184	149
Nb	19	27	33	56	53	71	61
Y	28	35	40.6	67	61	83	75
Hf	5.7	5.9	6.28	8	5.9	10.1	8.1
Th	26.7	26	22.66	31.2	30	35.8	29
Ga	18.8	20.2	21.4	26.2	24.5	28.4	29
Ta	5.6	9.3	3.03	8	3.9	5.1	5
Sc	2.47	2.7	4.1				
Pb							
La	35	41	32	26	17.6	29	26
Ce	79	87	72	67	40.2	68	72
Pr	8.9	10.4	8.6	8.4	6.5	8.9	8.5
Nd	31	37	31	31	26	32	31
Sm	6.4	7.6	6.55	8.31	7.35	9.46	8.79
Eu	0.62	0.67	0.5	0.14	0.18	0.07	0.08
Gd	5.03	6.08	5.48	8.64	7.17	9.83	8.46
Tb	0.82	1	0.92	1.62	1.36	1.89	1.74
Dy	4.82	5.85	5.79	10.23	8.43	12.48	10.97
Ho	0.92	1.13	1.33	2.2	1.83	2.79	2.29
Er	2.83	3.26	3.63	6.5	5.77	7.46	6.79
Tm	0.48	0.63	0.58	1.02	0.91	1.16	1.02
Yb	3.22	4.14	3.86	7.22	6.7	7.48	7.36
Lu	0.46	0.57	0.57	1.03	0.96	1.1	1.03
Eu/Eu*	0.32	0.29	0.25	0.05	0.07	0.02	0.03
$(La/Yb)_N$	7.21	6.49	5.42	2.40	1.73	2.52	2.36

Eu/Eu* = $Eu_n/(Sm_n*Gd_n)1/2$; NK/A = $(Na_2O+K_2O)/Al_2O_3$, mol.%; 1.6* = Fe total as Fe_2O_3 in the Katherina pluton. AG-41MP—data of microprobe analysis.

TABLE 7

Homogenization temperature (T_h) of melt inclusions in quartz from felsic rocks of the Katherina Ring Complex

Rock groups	Rock types	T_h max, °C	T_h < max, °C	Sample numbers
Volcanic rocks	PA ignimbrite	780-800		AG-41, AG-42
Wadi Shagar Musa body	PA granite	880	620	AG-55,AG-139
upper part		780-830	670-710	AG-138, AG-193
		880	830	AG-50
Shagar Musa lower part		990	660-700	AG-150
Gebel Musa		880	620	AG-58
IRD, Wadi Jarjaniya body	Kataphorite Ab-Afs microgranite	990	780	AG-9, AG-11
ORD	PA perthite granophyre	830	660-700	IL-73
	Afs quartz syenite	830	650-700	IL-125
Katherina pluton	Syenogranite	720	670	D-9
	Perthite granite	750-780	630-650	D-40, D-43

T_h max = the highest homogenization temperature; in volcanic and dike rocks, T_h max ~ T_{liq}.
T_h < max = homogenization temperature supposedly marking crystallization of quartz within the liquidus-solidus interval.

The REE patterns of peralkaline granites are almost parallel to those of the syenogranite and the AFS granite of the Katherina pluton (fig. 8D). The main distinction is the lower content of LREE and, less clear, HREE in the pluton rocks.

There are a number of chemical distinctions between the Katherina pluton granites and the volcanic and ring dike rocks with similar silica content (≥ 71 wt.% SiO_2). The granites of the pluton have lower agpaitic indices $(Na_2O+K_2O)/Al_2O_3$ (fig. 6B), as well as lower LREE (fig. 8 D), Zr, Hf and Na_2O contents (fig. 9). The compositional trends for Sr, Eu/Eu*, CaO, as well as for MgO and FeO^T (not shown) in high silica silicic subvolcanic rocks and plutonic granites do not overlap, although they are sub-parallel (fig. 9). This argues against a common parental magma for the two rock groups. The extremely low Eu/Eu* ratios of <0.1 in some peralkaline granite and ignimbrite (table 6) could not be caused by simple fractional crystallization of feldspars alone. It was shown by Jahn and others (2001) for a wide spectrum of highly alkaline granites that an additional process, such as end-stage melt-fluid interaction, must have been involved in enhancing the Eu depletion. This is commonly observed in granitic rocks with the REE tetrad effect. Such an effect is also distinguished in the AFS granite of the Katherina pluton (Katzir and others, 2007). This is manifested by the very low ratios of Eu/Eu* (0.02-0.05), (La/Yb)n (2.4).

DATA FROM MELT INCLUSION STUDY

Melt inclusions trapped by growing magmatic minerals can provide important information about the crystallization temperatures of magmas (Roedder, 1979; Reyf, 1997; Thomas and Klemm, 1997; Webster and Rebbert, 2001). We studied homogenization temperatures of melt micro-inclusions (≤5 μm) in quartz by heating to magmatic temperatures (see the analytic technique and references in the Appendix). The study was performed on quartz phenocrysts from volcanic and subvolcanic rocks and in quartz grains from plutonic syenogranite and perthite granite. Quartz from the matrix of Pl-bearing quartz syenite was not investigated because it crystallized at near-solidus temperature. The results are given in table 7. The data demonstrate a wide range of homogenization temperatures even in a single rock type. This is not

surprising because crystallization of quartz in highly silicic magmas can occur within almost the entire liquidus-to-solidus interval (Johannes and Holtz, 1996).

The study showed that in quartz phenocrysts from volcanic and subvolcanic rocks the maximum homogenization temperatures of melt inclusions vary from about 780 °C to 990 °C, whereas in the plutonic granite the range is comparatively narrow, from 720 to 780 °C (table 7). Significant differences in sub-liquidus temperatures established in quartz from volcanic and plutonic rocks is a widely known phenomenon (Jahn and others, 2009). In high silica A-type magmas, quartz is a liquidus mineral at the enhanced depth of magma generation (Johannes and Holts, 1996). However, it is unlikely that in plutonic rocks the early quartz that crystallized within or near the magma chamber could persist during the emplacement at shallow depth and slow equilibrium crystallization. Therefore, the data on the sub-liquidus temperatures obtained from the melt inclusion study in plutonic rocks characterize the temperature regime at the level of the pluton emplacement, but not the temperature of magma in the source region. In contrast, in the extrusive and subvolcanic rocks the early crystals may be preserved owing to the rapid ascent and solidification of magma at or near the surface. As magma ascends, its crystallization continues. Therefore quartz crystals formed at different depths and temperatures may be present in the same sample. In addition, the early quartz crystals could be overgrown with the later lower temperature zones. This is why only melt inclusions in phenocryst cores that have the highest temperature of homogenization can be considered to evaluate the magma temperature in the chamber. The highest T_{hom} determined in the quartz phenocryst cores from the subvolcanic peralkaline granite and kataphorite Ab-Afs microgranite samples (990 °C) suggest that the temperature of the silicic magma near the magma chamber was about 1000 °C (table 7). Similar and even higher values, up to 1100 °C, were reported for melt inclusions trapped in quartz phenocrysts from the comendite and pantellerite related to the peralkaline granitoid plutons in central Transbaikalia (Kuzmin and others, 1999; Litvinovsky and others, 2001; Reyf, 2004; Jahn and others, 2009) and in pantellerite from the Pantelleria Island (Kovalenko and others, 1994). Comparable temperatures in the range of 950 to 1050 °C were obtained for A-type charnockite magmas (Bonin, 2007).

DISCUSSION

Geochronology of Main Magmatic Events

The voluminous post-collisional magmatism in the northernmost ANS started at 635 to 620 Ma with intrusion of numerous calc-alkaline plutons along with their surface manifestations such as the early variants of the Dokhan Volcanics in the Eastern Desert and Ferani Group volcanics in Sinai, including the Rutig volcano-sedimentary succession that comprises the country rocks of the KRC (table 8). The peak in magmatic activity (610-600 Ma) is associated with a change of calc-alkaline magmatic rocks towards dominantly granitic composition. In addition, this period marks the contemporaneous beginning of extensive alkaline intrusive and extrusive magmatism (Jarrar and others, 2003; Ali and others, 2009; Be'eri-Shlevin and others, 2009a, 2011; Moreno and others, 2012).

Field relations indicate that formation of the KRC followed the Rutig volcano-sedimentary succession and intrusion of the Sulaf and Abu-Khsheib calc-alkaline plutons (fig. 1). Although Samuel and others (2011) and Be'eri-Shlevin and others (2011) claimed that evolution of the Rutig succession continued till 600 Ma, we are apt to argue that a more conservative estimate of 605 Ma, which is close to the age of the youngest dated volcanic rock of the Rutig Formation (table 8), is more appropriate. This also leaves a few m.y. for folding and erosion of the succession prior to the extrusion of the KRC Jarjaniya volcanics.

TABLE 8

Geochronology of the Katherina Ring Complex and country rocks

Complexes	Unit	Sample No.	Rock type	Age	Ref.	Remarks	UTM
Katherina Ring Complex	Katherina pluton	DV-82-87		583±5.6 Ma	(2)		
		KA-6	Syenogranite	597±7 Ma	(4)		N28°36′08.2″ E34°01′10.3″
		KA-12	Syenogranite	595±4 Ma	(4)		N28°36′45.1″ E34°01′26.5″
		KA-37		596±7 Ma 3.24±0.03 Ga	(4)	9 grains, 1 xenocryst	N28°32′44.4″ E33°57′16.5″
		KA-20	Alkali-feldspar granite	597±6 Ma	(4)		N28°28′18.4″ E33°59′32.7″
	Gebel Musa subvolcanic body	KA-30	Peralkaline granite	593±2 Ma	(4)		N28°32′18.6″ E33°58′30.7″
	Outer ring dike			601±5 Ma	(4)	single grains	N28°34′54.45″ E34°02′1.2″
	Inner ring dike	KA-32	Quartz-syenite	602±4 Ma	(4)		N28°32′1.05″ E33°58′26.2″
Country rocks inside the KRC	Abu Khsheib pluton	S-2695	Quartz monzonite	592±7 Ma	(2)		
		KA-29	Quartz monzonite	599±3 Ma	(4)	Isbaiya Unit, after Moreno and others, 2012	N 28°33′19.4″ E34°00′30.2″
	Moneiga pluton		Quartz diorite	844±4 Ma	(1)	The Moneiga pluton intrudes Rutig Formation volcanic rocks N of Gebel Musa, therefore 844 Ma cannot represent the intrusion age	
	Rutig Formation	V-16	Dacite	611±4 Ma	(3)	Upper Rutig in the paper, middle Rutig (our observations)	

TABLE 8
(continued)

Complexes	Unit	Sample No.	Rock type	Age	Ref.	Remarks	UTM
Country rocks inside the KRC	Rutig Formation	V-15	Dacite	607±3 Ma	(3)	Upper Rutig in the paper, middle Rutig (our observations)	
	Rutig Formation	V-17	Rhyodacite	623±4 Ma	(3)	Lower Rutig in the paper, middle Rutig (our observations)	
	Rutig Formation	32	Rhyolite	619±4 Ma	(3)	Lower Rutig in the paper, middle Rutig (our observations)	
	Rutig Formation	R-1	Congl.omerate polimict clast and matrix	620-970 Ma	(5)	72 grains; 620-640; 710-800; 930-970. Lower Rutig in paper, upper Rutig (our observations)	
	Rutig Formation	Rb-4a	Conglomerate granite cobble	614±6 Ma	(5)	28 grains; middle Rutig in the paper, upper Rutig (our observations)	
	Rutig Formation	Rb-4b	Conglemarte matrix of Rb-4a	595-975 Ma	(5)	19 grains; 595-640; 740-860; 952-975.	
	Rutig Formation	Rb-1	Conglomerate dacite cobble	629±8 Ma	(5)	5 grains; upper Rutig	
	Rutig Formation	KA-14	Biotite monzogranite boulder	623±3 Ma 741±15 Ma Xenocryst	(4)	Collected above sample KA-23	N 28°28′18.4″ E33°59′32.7″
	Rutig Formation	KA-15	Biotite monzogranite boulder	735±6 Ma	(4)		
	Rutig Formation	KA-16	Biotite monzogranite boulder	748±11 Ma	(4)		
	Rutig Formation	KA-23	Rhyodacite, volcanic flow	622±3 Ma	(4)	Lower part, above the granite	N28°28′22.1″ E33°59′26.0″

Table 8
(continued)

Complexes	Unit	Sample No.	Rock type	Age	Ref.	Remarks	UTM
Country rocks inside the KRC	Rutig Formation		4 rhyodacites, one dacite, and one basalt	621±15 Ma Io=0.7031±3	(4)		
Country rocks outside the KRC	Sulaf Complex	S-2199		597±4.9 Ma	(3)	North of the KRC	
	Rahba pluton	S-2069		610±4.8 Ma	(3)	South of the KRC	
	Hibran-Miar Complex			619±4 Ma	(3)	SW of the KRC	

(1) Bea and others, 2009; (2) Be'eri-Shlevin and others, 2009a; (3) Be'eri-Shlevin and others, 2011; (4) Moreno and others, 2012; (5) Samuel and others, 2011.

The zircon U-Pb age data for the calc-alkaline Abu Khsheib (Isbaiya) pluton of Moreno and others, 2012), indicate that the age of the pluton should be considered to be about 599 ± 2 Ma given by Moreno and others (2012) rather than 592 ± 7 Ma age reported by Be'eri-Shlevin and others (2009a). This is consistent with the reported intrusion age of 597 ± 5 Ma for the Sulaf pluton (Be'eri-Shlevin and others, 2009a) located immediately to the north of the KRC (fig. 1).

Focusing on the time scale for the evolution of the KRC, the weighted average $^{206}Pb/^{238}U$ ages for the ORD and for a quartz syenite (correlated to the IRD) reported by Moreno and others (2012) at 601 ± 5 Ma and 602 ± 4 Ma respectively constrain the evolution of the complex to about 600 Ma. These ages provide minimum constraints for the extrusion of the hitherto undated volcanic succession of the Jarjaniya Formation, which comprises the earliest part of the KRC. Considering the overlapping ages, within a level of confidence, of the latest calc-alkaline plutons and those of the ring dikes of the KRC, as well as the constraints given by the age of the youngest Rutig volcanics (607 Ma), the age of the Jarjaniya Formation cannot be much older than 600 Ma. The formation of the KRC ended with intrusion of the Katherina pluton. Be'eri-Shlevin and others (2009a) reported a ^{207}Pb corrected age of 583 ± 6 Ma for this pluton. However, new robust zircon U-Pb data by Moreno and others (2012) (49 analyses on 46 grains; 3 different samples) suggest that the age of the Katherina pluton is older, *ca.* 596 Ma. This new estimate indicates an evolution period of the KRC on the order of 5 m.y., consistent with evaluations of Moreno and others (2012). These workers also reported a *ca.* 593 Ma age for the Gebel Musa peralkaline subvolcanic body and considered this to indicate a significantly younger magmatic phase of KRC. Our field observations, however, indicate that this body is intruded by the IRD (quartz monzonite) and the Katherina pluton. Taking the age of the Katherina granite as 596 Ma, and quartz syenite–IRD as *ca.* 600 Ma (Moreno and others, 2012), the Gebel Musa subvolcanic body should be older than 596 to 600 Ma and does not comprise the youngest magmatic event of the KRC.

To sum up, the most realistic time interval of the KRC formation is from ~600 Ma to 595 Ma, which corresponds to a period of highly pronounced extensional regime in the within-plate setting. The latest extensional episode in the Ediacaran magmatic activity that caused the silicic melts intrusion occurred at 592 ± 6 Ma and was exhibited in formation of abundant dike swarms (alkaline rhyolite and rhyolite-trachydolerite composite dikes) throughout Sinai and southern Israel (Katzir and others, 2006; Be'eri-Shlevin and others, 2009a).

Temperatures of the Granitoid Magmas

Temperatures of magmas were estimated based on the mineral thermometers (clinopyroxene, ternary feldspar) and melt inclusion studies. The highest values, about 900 to 1100 °C, are obtained for clinopyroxenes in the quartz monzonite from the ring dikes (fig. 4). It was shown above that augite and pigeonite are early minerals that may represent the temperature in the magma chamber just before emplacement.

Ternary feldspar phenocrysts in quartz monzonites provide temperature estimates that characterize the intermediate part of the liquidus-solidus interval, after crystallization of plagioclase. The location of the ternary feldspar compositions in the Ab–An–Or diagram with solvus isotherms at P = 2 kbar (Lindsley and Nekvasile, 1989; Nekvasile, 1992) indicates a temperature range from 760 to 900 °C, primarily from 840 to 900 °C (fig. 5). This suggests that the liquidus temperature of the quartz monzonite melt exceeded 900 °C in the process of emplacement.

The melt inclusion study gives results consistent with those from the mineral thermometers (table 7). The highest homogenization temperature (T_{hom}) determined in the quartz phenocryst cores from the subvolcanic peralkaline microgranite

(990 °C) suggests that the temperature of the silicic magma near the magma chamber was about 1000 °C.

Thus, estimation of silicic magma temperature in the KRC volcanic and dike rocks points to fairly high temperatures, 900 to 1000 °C, of magma generation, which is characteristic of a lower crust conditions and water-undersaturated melting. Crystallization temperature at a shallow depth of magma emplacement averages between 650 and 750 °C (table 7).

Petrogenetic Interpretation Based upon the Isotope and Elemental Geochemistry Data

Isotope compositions.—Isotope compositions are commonly considered as the most powerful tracer for distinguishing between crustal and mantle-derived magma sources. However, in regions dominated by young juvenile crust, such as the Arabian-Nubian Shield, petrogenetic interpretation of isotope data can be ambiguous (Stern, 2002; Hargrove and others, 2006; Liégeois and Stern, 2010). A compilation of the available Sm-Nd isotope data for ~120 samples of igneous and metamorphic rocks from southern Israel, southwestern Jordan, Sinai Peninsula and Eastern Desert, Egypt (Eyal and others, 2010) demonstrated that the isotopic data do not provide a clear answer regarding the generation of the silicic magmas, either directly from the upper mantle, or from melting of young juvenile crust. They do allow, however, identification of the ancient continental crust contribution. The $\varepsilon_{Nd}(T)$ values are always positive, and the Nd model ages of the island arc and post-collisional Neoproterozoic igneous rocks from the northern ANS show a similar range from *ca.* 800 to 1200 Ma (Eyal and others, 2010, see Online tables 2-SD, http://earth.geology.yale.edu/~ajs/SupplementaryData/2013/05EyalSD-2.doc and 4-SD, http://earth.geology.yale.edu/~ajs/SupplementaryData/2013/07EyalSD-4.doc). This suggests that little or no early Proterozoic or older continental crust exists in the middle to lower crust of the northern ANS. In fact, this inference is supported by the absence of zircon xenocryst U-Pb ages older than 900 Ma in all plutonic rocks from the Sinai Peninsula (Be'eri-Shlevin and others, 2009a), and by radiogenic Sm/Nd isotope studies of Neoproterozoic granite gneiss in the Eastern Desert, Egypt (Liégeois and Stern, 2010). Mesoproterozoic volcanic arc zircon ages (1000-1100 Ma) are known only in the Sa'al area in central Sinai (Be'eri-Shlevin and others, 2012).

The original magmatic $\delta^{18}O$ value of zircon [$\delta^{18}O(Zrn)$] might have been preserved even in the rocks that have undergone hydrothermal alteration and high temperature metamorphism (Valley, 2003). The igneous zircons in equilibrium with mantle-derived magma have an average $\delta^{18}O(Zrn) = 5.3 \pm 0.6$ permil (2δ; Valley and others, 1998). Be'eri-Shlevin and others (2009b) measured oxygen isotope ratios in bulk zircon separates of ca. 40 plutons of southern Israel and Sinai. The $\delta^{18}O(Zrn)$ data of the post-collisional calc-alkaline and alkaline intrusive rocks show indistinguishable average $\delta^{18}O(Zrn)$ values: 5.7 permil and 5.8 permil respectively. This indicates that both the calc-alkaline and alkaline magmas were derived from sources with mantle-like $\delta^{18}O$ values, further implying a mantle or young juvenile crust source.

Oxygen isotope studies performed in the KRC yielded results which are consistent with those for the region as a whole (for example, Be'eri-Shlevin and others, 2009b): the $\delta^{18}O(Zrn)$ values for the ring dikes are 5.53 ± 0.09 permil, for the Katherina pluton granite 5.82 ± 0.06 permil and for the calc-alkaline Abu Khsheib pluton, intruded by the ORD (fig. 1), 5.25 ± 0.04 permil. All these data attest to the minor, if any, role of the ancient continental crust material in formation of the KRC granitoid magmas.

The Nd isotope data, unlike the oxygen isotope ratios, show some systematic distinctions between various rock types of the Katherina Ring Complex. As presented in table 9, three groups of rocks can be distinguished by the $\varepsilon_{Nd}(T)$ values (Katzir and others, 2007; Eyal and others, 2010): (1) quartz monzonite ($\varepsilon_{Nd}(T) = 5.4$ and 5.5); (2)

TABLE 9

Sm-Nd isotope data for the Katherina Ring Complex (595 Ma)

Sample no.	Rock type	SiO_2	[Sm]	[Nd]	$\frac{^{147}Sm}{^{144}Nd}$	$\frac{^{143}Nd}{^{144}Nd}$	±2σ	$\varepsilon_{Nd}(0)$	$\varepsilon_{Nd}(T)$	$f_{Sm/Nd}$	T_{DM}-1	T_{DM}-2
IL-66 [1]	quartz monzonite	61.2	10.97	62.42	0.1062	0.512571	3	-1.3	5.5	-0.46	822	911
IL-189 [3]	quartz monzonite	62.5	8.45	46.9	0.1088	0.512591	3	-0.9	5.4	-0.45	813	841
IL-161 [1]	quartz syenite	64.19	12.08	72.82	0.1003	0.512503	3	-2.6	4.6	-0.49	870	932
AG-32 [1]	PA granite	75.35	12.17	63.49	0.1159	0.512558	3	-1.6	4.5	-0.41	923	945
AG-41 [3]	PA ignimbrite	76.05	13.79	64.9	0.1284	0.512591	3	-0.9	4.2	-0.35	999	956
D-165 [1]	syenogranite	76.41	7.26	36.33	0.1208	0.512546	3	-1.8	3.9	-0.39	991	971
D-163 [1]	syenogranite	74.11	6.34	32.57	0.1176	0.512519	3	-2.3	3.6	-0.40	1002	1010
D-54 [3]	AFS granite	76.91	4.94	17.91	0.1744	0.512714	6	1.5	3.2	-0.11	1689	775
D-43 [2]	AFS granite	76.82	5.82	18.28	0.1925	0.512754	5	2.3	2.6	-0.02	2827	736

Superscripts in the sample numbers denote the data cited from Katzir and others, 2007([1]), Eyal and others, 2010 ([2]), and present new unpublished data ([3]).

Isotope ratios were measured at the Universite de Rennes, France, and at the Institute of Earth Sciences, Academia Sinica, Taipei.

CHUR (chondritic uniform reservoir): $^{147}Sm/^{144}Nd = 0.1967$; $^{143}Nd/^{144}Nd = 0.512638$. Used in model age calculation, DM (depleted mantle): $^{147}Sm/^{144}Nd = 0.2137$; $^{143}Nd/^{144}Nd = 0.51315$. $T_{DM}-1 = 1/1 \times \ln[1+(0.51315-(^{143}Nd/^{144}Nd)_s)/(0.2137-(^{147}Sm/^{144}Nd)_s]$. $T_{DM}-2 = [(e_{DM} - e_{sample} + QT_c(f_s - f_{cr})]/Q\ (f_{DM} - f_{cr})$, where $e_{DM} = 10$, $f_{DM} = 0.086$, $f_{cr} = -0.4$, and $Q = 25.1$. Thus $T_{DM}-2 = [(10 - e_{sample} + 25.1T_c(f_s+0.4)]/[25.1(0.086+0.4)]$.

All in-run errors of isotopic ratios represent 2 standard errors, and correspond to the last decimal points of the reported ratios.

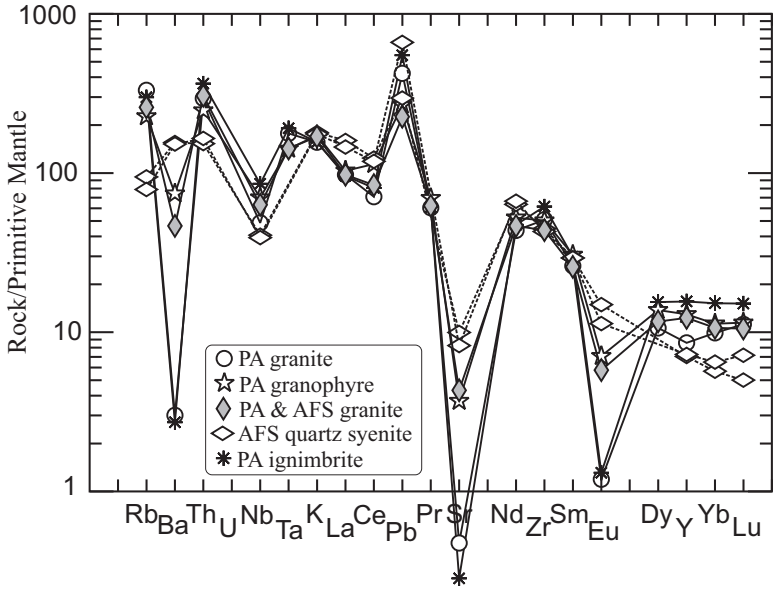

Fig. 10. Primitive mantle-normalized multi-element diagram, illustrating systematic change of trace element abundances in the rock sequence from AFS quartz syenite to highly differentiated PA granite and rhyolite. Primitive mantle values after Sun and McDonough (1989).

PA ignimbrite, PA granite and quartz syenite (4.2-4.6), and (3) syenogranite and AFS granite making up the Katherina pluton (2.6-3.9). The difference in Nd isotopic compositions between the groups exceeds the error limit. The model ages (T_{DM}-2) of all the Katherina rocks vary from 750 to 1000 Ma. The initial $^{87}Sr/^{86}Sr$ ratios calculated for individual samples range from 0.70300 to 0.70372 (Katzir and others, 2007). The positive $\varepsilon_{Nd}(T)$ values suggest that the three groups of rocks were derived from sources with mantle-like $\varepsilon_{Nd}(T)$ values. The distinction between them probably suggests that the rocks were derived from heterogeneous sources or their generation involved a more complicated process.

Elemental geochemistry.—The geochemical data can be used to discuss possible models of petrogenesis for the KRC rocks. As shown in the Geochemistry chapter, the data points form two trends, a steeply dipping and a gently sloping, in the silica variation diagrams (figs. 7C-7F). Compositions of the evolved silica-rich rocks are confined to the gently sloping trend. The trend begins from the AFS quartz syenite with a Eu/Eu* ratios of 0.62 to 0.47 (fig. 7C), then followed by the AFS and PA subvolcanic granitoids and PA rhyolitic ignimbrite as silica increases (figs. 7C-7F). The compositional changes in this rock series, demonstrated by the gently sloping trend, are consistent with a model of fractional crystallization of the AFS quartz syenite magma. This interpretation is supported by the data from the primitive mantle-normalized multi-element diagram (fig. 10). In the rock sequence from AFS quartz syenite to highly differentiated PA granite and rhyolite with Eu/Eu* ratio <0.1, the significant decrease of Ba, Sr, La, Eu, and concurrent increase of Rb, Th, Nb, HREE abundances suggest fractionation of feldspars and mafic minerals and accompanying enrichment of the residual melt in silica, and large-ion lithophile (LIL) and high field-strength (HFS) elements.

The steeply dipping trends in figures 7C–7F mark a compositional change in the quartz monzonite-syenite group and AFS quartz syenite, mostly with the enhanced

Eu/Eu* ratios of 0.72 to 0.88 (fig. 7C). Quartz monzonite and Pl-rich quartz syenite, the dominant rock types of the ring dikes and subvolcanic Abbas Pasha body (fig. 1), contain varying amounts of cumulate crystals, first of all plagioclase $An_{28\text{-}35}$. This is manifested in the elevated Eu/Eu* ratios attaining 1.63 (figs. 7C and 8B). It is likely that the accumulated mafic mineral was clinopyroxene, which was extensively replaced by magnesio-hornblende.

Thus, based on the chemical data, the quartz monzonite-syenite rock type of the KRC cannot be interpreted as a low-silica melt that was parental to the more silicic rocks of the complex. The quartz monzonite and Pl-rich quartz syenite varieties correspond to the composition of a crystal "mush" with varied proportion of accumulated plagioclase and, possibly pyroxene. The transition from the relatively high Eu/Eu* ratios (up to 0.88) to the lower Eu/Eu* ratios (~0.5) in the AFS quartz syenite (fig. 7C) suggests that the latter also contains accumulated feldspar crystals, mostly alkali feldspar.

The steeply dipping and gently sloping trends cross in the area of fractionated AFS quartz syenite compositions (figs. 7C-7F). This suggests that the AFS quartz syenite magma could be parental to the high silica alkaline–peralkaline rocks, whereas similar quartz syenite magma, subjected to mixing with the mafic magma, was enriched in accumulated crystals, which resulted in formation of hybrid quartz monzonite. Indeed, the quartz monzonite, except of corroded plagioclase and pyroxene crystals, consists of 40 to 50 percent alkali feldspar phenocrysts and a microgranite matrix with noticeable proportion of small plagioclase, amphibole, biotite and Fe-Ti oxide grains. The latter suggests that hybridization of the quartz syenite magma was manifested not only in the appearance of accumulated crystals, but also in the enrichment of the hybridized silicic melt in Mg, Fe, and Ti. The steeply dipping curves in figures 7C–7F can be interpreted as trends of decreasing proportion of the accumulated crystals in the magmas. Taking the plagioclase phenocrysts in quartz monzonite as an example (fig. 6), a dramatic disequilibrium between the accumulated crystals and the host melt can be observed from the extensive interaction between these phenocrysts and the microgranitic matrix. The interaction has resulted in the corrosion of crystals, the formation of alkali feldspar reaction rims, and the replacement of plagioclase by alkali feldspar. Calcium consumed by the enclosing melt caused formation of small An_{14} crystals in the crystallized matrix.

The source of the accumulated crystals is a matter of debate. It is unlikely that the andesine and Ca-rich pyroxene are related to the AFS quartz syenite magma, accumulated by settling in the base of the same batch of magma. More probable is the assumption that the initial quartz syenite magma was hybridized by admixture of partly crystallized mafic magma (monzonite, monzodiorite). The noticeably larger $\varepsilon_{Nd}(T)$ values in the quartz monzonite as compared with the rest of the subvolcanic rocks (table 9) supports such an assumption, although we have to remember that rocks with $SiO_2 < 61$ weight percent are not known in the KRC. Injection of hot mafic magma in the partially crystallized AFS quartz syenite magma would result in an increase temperature, repeated partial remelting and mixing-mingling of two magmas.

To explain anomalously enhanced Eu/Eu* ratios in the quartz monzonite, we should consider two possible scenarios: (1) The hybrid magma contained a significant proportion of crystal phase, including plagioclase from both end-members: $An_{30\text{-}34}$ and $An_{20\text{-}24}$. In the course of crystallization plagioclase and mafic minerals settled and accumulated in the deeper levels of the magmatic bodies; these levels are currently exposed. (2) The mafic magma was enriched in the plagioclase crystals still before mixing. This might occur in the upper part of the monzodiorite/monzonite magmatic reservoir owing to the andesine buoyancy in a mafic magma. Injection of such monzodiorite crystal "mush" into the AFS quartz syenite magma would result in

formation of a hybrid melt with abundant crystal phase enriched in plagioclase. Further evolution of this hybrid mixture, possibly via fractional crystallization, would bring about formation of the quartz monzonite—quartz syenite—granite sequence observed in the Outer Ring Dike.

Direct genetic relationships between the alkaline granites making up the Katherina pluton and the alkaline-peralkaline subvolcanic granite, quartz syenite and rhyolite is unlikely. The chemical distinctions between these rock groups were discussed in the Geochemistry chapter and illustrated in figure 9. These data are supported by distinct $\varepsilon_{Nd}(T)$ values, 4.2 to 4.6 in leucocratic subvolcanic rocks and 2.6 to 3.9 in plutonic syenogranite and AFS granite (table 8). The possibility that the pluton formed from a new batch of magma that replenished the magmatic chamber and maybe mixed with the melts that remained within the chamber seems the most plausible.

A Model for the Residual Melt Extraction

It was shown in the foregoing sections that fractional crystallization was likely the main process that caused the formation of the high-silica rock sequences in the KRC, from the alkali feldspar quartz syenite to peralkaline granite and ignimbrite.

In the Katherina pluton the same process was dominant in the formation of the residual alkali feldspar granite melt from the crystallizing syenogranite magma (Katzir and others, 2007). The special feature of the pluton is vertical zoning, from syenogranite upward to alkali feldspar granite. The contacts between different zones are gradational. These relationships suggest that differentiation occurred at the level of the syenogranite magma emplacement rather than in the deep magma chamber. Taking into account a shallow depth of the pluton emplacement and crystallization, as well as high viscosity of silicic magma, it is difficult to conceive of such a high extent of magma differentiation via crystal settling. A model of the residual silicic melt extraction from the magmatic "mush" was suggested and discussed in our previous work (Katzir and others, 2007). In brief the model is as follows. According to mass balance calculations, the residual melt that produced the alkali-feldspar granite was separated from the syenogranite crystal "mush" with 50 to 55 percent of the crystal phase (plagioclase, alkali feldspar, quartz, secondary biotite). The crystal proportion corresponds to the so called "rigid percolation threshold" (Van der Molen and Peterson, 1979; Vigneresse and others, 1996). At this stage the crystals construct a rigid skeleton in the magma; clusters of crystals can be deformed, but still sustain stress. The residual melt may flow pervasively through pore space or fracture network (Brown and Solar, 1999; Weinberg, 1999; Leitch and Weinberg, 2002). Thus the residual melt of alkali-feldspar granite composition could be extracted from the crystal "mush" and flow upward. The essential driving force of such flow was decrease of pressure from fracturing of the roof (Bons and others, 2004).

A similar mechanism seems to be appropriate for describing the separation of silica-rich residual magmas formed in the course of fractional crystallization of the initial AFS quartz syenite magma at the earlier, subvolcanic stage of the KRC formation. The distinctive feature of this stage is that separation of the residual melt could have occurred at a wide range of depths (in the magmatic chamber and intermediate intra-crustal reservoirs), which resulted in the separation, intrusion and extrusion of the separated melts.

We can also assume that a similar differentiation-extraction model caused separation of quartz syenite residual melt from the incompletely crystallized quartz monzonite magma in the ring dikes and formation of quartz syenite lenses, enclaves, strips, dikes and possibly even the large dike-like quartz syenite body in the southern part of the ORD (fig. 1).

The suggested model of melt separation alleviates the problem of differentiation in the fractional crystallization process: this model does not require crystal settling that seems unrealistic in highly viscous silicic magmas.

Origin of Perthitic (Hypersolvus) and Two-Feldspar albite-perthite (subsolvus) Granites in the Katherina Pluton and Wadi Shagar Musa Body

It was shown in Chapters 2 and 3 that in the Wadi Shagar Musa body and in the Katherina pluton both hypersolvus (perthite) and subsolvus (two-feldspar albite—perthite) granitic rocks are present. The hypersolvus granite forming the upper zone is changed gradually to the subsolvus granite type at the deeper level, without a noticeable change in chemical composition (table 6; see also Katzir and others, 2007). The type of granite strongly depends on the water pressure during crystallization: hypersolvus rocks crystallize from magma with low water fugacity, whereas subsolvus granite formed from magma enriched in water. In particular, for the haplogranite system the critical P_{H_2O} must be ≥3.5 to 4 kbar (Yoder and others, 1957; Johannes and Holtz, 1996). However, it was demonstrated by James and Hamilton (1969) that crystallization of two feldspars occurs at lower P_{H2O} if the system contains small amounts of An and fluorine. Kovalenko (1978) demonstrated that crystallization of a low-Ca granite system (0.11-0.42 wt.% CaO) resulted in formation of two feldspars at P_{H_2O} = 1 kbar when the fluorine concentration was ≥0.1 weight percent. Similar chemical features are characteristic of alkaline and peralkaline granites from the KRC. The amount of CaO ranges from 0.1 to 0.4 weight percent (table 6). Fairly high F contents in amphibole and biotite from the subvolcanic rocks, 1.06 to 1.7 weight percent (tables 4 and 5), ~3 weight percent F in biotite and abundance of fluorite in the perthite granite of the Katherina pluton (Katzir and others, 2007) attest that silicic magmas were moderately enriched in fluorine. The inference that the granite magmas were H_2O-enriched follows from the evidence that they were formed as residual melts produced in the process of highly evolved fractional crystallization of the alkali feldspar quartz syenite magma. Crystal fractionation provided enrichment of the residual melt in water, which is exhibited in anomalously low Eu/Eu*, <0.1 ratios indicating melt-fluid interaction in the near-solidus conditions (see above, chapter Geochemistry). Based on these data, the following hypothesis for the two zones formation is suggested.

When the evolved, water-enriched granite magma was emplaced in the highly fractured volcanic edifice at shallow depth less than 2 to 3 km, it was subjected to quick crystallization accompanied with extensive loss of H_2O-fluids. This brought about formation in the uppermost part of the pluton of a hypersolvus perthite granite "plug" that prevented the fluid flux from magma into the roof. Accumulation of fluids below the perthite granite plug caused P_{H_2O} increase and crystallization of two-feldspar (subsolvus) granite.

CONCLUSIONS

The available data allow us to recognize four main stages of the Katherina Ring Complex (KRC) formation during the period of ~600 to 595 Ma:

1. In a quartz syenite—AFS quartz syenite magma chamber, the fractional crystallization process brought about production of H_2O-enriched high silica alkaline and peralkaline magmas in the upper level of the chamber. Explosive eruption of rhyolitic breccia and ignimbrite was followed by PA ignimbrite. At the end of this stage peralkaline silicic magma was emplaced in the volcanic edifice, forming the Wadi Shagar Musa subvolcanic body and associated minor intrusions. In the Wadi Shagar Musa body, perthitic (hypersolvus) PA granite formed in the upper part and two-feldspar albite-perthite (subsolvus) PA granite crystallized in the lower part.

2. A batch of high-temperature monzonite/monzodiorite magma intruded into the granitoid chamber causing partial remelting of the incompletely crystallized host quartz syenite magma. Mingling and mixing processes produced the hybrid quartz monzonite magma (magmatic "mush") in the lower part of the chamber. Emplacement of the hybrid quartz monzonite magma produced the Abbas Pasha subvolcanic body, and the Inner and Outer ring dikes.

3. In the eastern part of the Outer Ring Dike the post-monzonitic stage of fractional crystallization of the AFS quartz syenite magma was manifested by and resulted in production of granite melts. The younger perthite and peralkaline granite were intruded into the quartz monzonite.

4. A latest batch of granitic magma replenished the magmatic chamber and was emplaced in the volcanic caldera and older Neoproterozoic rocks outside the caldera as the Katherina pluton. In the course of the syenogranite magma crystallization, part of the residual melt was extracted, transferred to the uppermost levels of the pluton and formed the alkali feldspar granite upper zone. This zone was divided into perthite (hypersolvus) granite in the upper part and two-feldspar albite-perthite (subsolvus) granite in the lower part.

Petrogenetic aspects of magma generation and crystallization:

A. The formation of various highly alkaline silicic magmas that produced the rock sequence from AFS quartz syenite (supposed initial silicic magma) to PA granite and ignimbrite is consistent with the model of fractional crystallization of the quartz syenite magma. This model is also appropriate for explaining the vertical zoning in the Katherina pluton, from syenogranite to alkali feldspar granite.

B. A specific feature of magma differentiation processes in the KRC is that the residual melts have been extracted from crystallizing bodies when the magma was ~55 percent crystallized ("rigid percolation threshold") and clusters of crystals formed a rigid skeleton in magma. Residual melt flowed pervasively through the pore space, and tectonic deformation further accelerated this separation of the melts. This type of separation can be carried out either "*in situ,*" at the emplacement level (the Katherina pluton) or at the greater depth, with subsequent emplacement of the separated evolved magma batches at shallow levels, as occurred during the formation of ring dikes in the KRC. The suggested model of melt separation alleviates the problem of differentiation in the fractional crystallization process as this model does not require crystal settling that seems highly improbable in viscous silica-rich magmas.

C. Quartz monzonite is distinguished by varying proportions of corroded and partially replaced $Pl_{28\text{-}35}$ and clinopyroxene crystals. The enhanced Eu/Eu* ratios, up to 1.63, and the highest positive $\varepsilon_{Nd}(T)$ values (5.4-5.5) in quartz monzonite suggest that at least part of the Pl and Cpx grains are actually xenocrysts captured in the process of mixing-mingling of the quartz syenite magma and monzonite/monzodiorite crystal "mush" enriched in Pl crystals.

D. A number of geochemical distinctions, including the clear difference in the $\varepsilon_{Nd}(T)$ values between the leucocratic volcanic, subvolcanic rocks (4.2-4.6) and the Katherina pluton granite (2.6-3.9) suggests that the silicic magmas of two successive stages were produced from different, although related sources.

ACKNOWLEDGMENTS

The authors are cordially grateful to Drs. I. Bruner and the late A. Goor for collaboration and valuable contribution, and to J. K. Hall for improving the English editing. Thoughtful reading and important recommendations of the Guest Editor G. Shellnutt, and the reviewers M. K. Azer and an anonymous reviewer enabled significant improvement of the manuscript. The investigations were financially supported by the

Ministry of Energy and Water Resources, Israel (grants ES-18-2008, ES-2-2010, ES-1-2012).

Appendix

Analytical Methods

Microprobe analysis.—Microprobe analysis (of rock-forming minerals was carried out with a JEOL JXA-8600 Electron Probe Microanalizer equipped with Tracor Northern TM 5500/5600 energy disperser and automation system at the Institute of Earth Sciences, a Hebrew University, Jerusalem, Israel. Quantitative mineral analysis was made with 15 keV acceleration voltage, 10.0 nA beam, focused to 2–3 μm. X-Ray spectra were collected via an Energy Dispersive Spectrometer (EGS) and Wave-length Dispersive Spectrometers (WDS). Data were reduced by the ZAF matrix correction procedure. The detection limits are 0.05–0.09 wt.% for Na_2O, MgO, Al_2O_3, and SiO_2; 0.01–0.05 wt.% for Cl, K_2O, CaO, TiO_2, MnO, FeO, and 0.3–0.4 wt.% for F.

Whole-rock chemical analysis.—Whole rock chemical analyses were performed at the Geological Survey of Israel by an ICP-AES (Perkin-Elmer; Elan 3000) for major elements and by an ICP-MS (Perkin-Elmer; Elan 6000) for trace elements (Rb, Sr, Ba, Y, Zr, Nb and REE). For the major element analysis, rock powders (0.5 g per sample) were fused with a flux $Li_2B_2O_4$ (1.25 g) in platinum crucibles and the melt was dissolved in 0.1N HNO_3. A 5 ppm aliquot of an internal Sc standard was added to each dissolved sample. For trace element analysis, rock powders (0.5 g) were sintered with Na_2O_2 (2 g) in zirconia crucibles at 500 °C followed by dissolution in 2N HNO_3. An internal standard solution of 10 ppb Rh + Re was added to each sample. International standards SO-3, NIM-G, NIM-L, BCR-32 and BHVO-1 were routinely measured during the ICP-AES analyses. Likewise ICP-MS measurements were standardized using SO-3 and JB-1 [see details in Eyal and others (2010); the results of the standards SO-3 and NIM-G analyses are given in table 1]. In selected samples whole-rock chemical analysis of major elements was performed at the Geological Institute of the Russian Academy of Sciences (Ulan-Ude) using a combination of photometry (SiO_2, TiO_2, Al_2O_3, P_2O_5), flame emission spectrometry (Fe_2O_3, MgO, CaO) and titration (FeO). All analyses are accurate to within 2–5% for major elements, and better than 10–15% for trace elements. The accuracy for all the REE (except Lu) is 1–5%; and for Lu, it is 9–10%.

Melt inclusion study.—This study was carried out at the Ben-Gurion University of the Negev, Beer-Sheva, Israel. The analytical procedures are described in detail and criteria for picking the most appropriate melt inclusions are discussed in Litvinovsky and others (2002; 2006), and Jahn and others (2009). Therefore only brief information is given below. Melt inclusions in quartz phenocrysts and grains were analyzed using a heating stage with a silicon-carbide heating element designed by A. Slutsky. The heating stage provides visual observation of the inclusion behavior upon heating to 1650 °C. The precision of temperature measurement is better than ±10 °C for the interval of 700–1000 °C. The homogenization temperatures (T_{hom}) were measured in groups of small inclusions (≤5 μm) because heating of larger inclusions usually causes partial loss of fluids and, as a result, overstating of homogenization temperature (for example, Reyf, 2004 and references therein). Results were considered reliable when, in a group of ≤10 small inclusions, the distinction in homogenization temperature values was less than 15 °C.

Online Supplementary Data

Table 1-SD. Modal mineral compositions of main subvolcanic rock types in the Katherina Ring Complex, http://earth.geology.yale.edu/~ajs/SupplementaryData/2013/04EyalSD-1.doc

Table 2-SD. Compositions of feldspars in main rock types of the volcanic and subvolcanic rocks from the Katherina Ring Complex, http://earth.geology.yale.edu/~ajs/SupplementaryData/2013/05EyalSD-2.doc

Table 3-SD. Microprobe analyses of Fe-Ti oxides in representative rock types of ring dikes from the Katherina Ring Complex (wt%), http://earth.geology.yale.edu/~ajs/SupplementaryData/2013/06EyalSD-3.doc

Table 4-SD. Chemical compositions of igneous rocks from the Katherina Ring Complex (all available data), http://earth.geology.yale.edu/~ajs/SupplementaryData/2013/07EyalSD-4.doc

References

Ali, B. H., Wilde, S. A., and Gabr, M. M. A., 2009, Granitoid evolution in Sinai, Egypt, based on precise SHRIMP U-Pb zircon geochronology: Gondwana Research, v. 15, n. 1, p. 38–48, http://dx.doi.org/10.1016/j.gr.2008.06.009

Bea, F., Abu Anbar, M., Montero, P., Peres, P., and Talavera, C., 2009, The ~844 Ma Moneiga quartz diorites

of the Sinai, Egypt: evidence for Andean-type arc- or rift-related magmatism in the Arabian-Nubian Shield?: Precambrian Research v. 175, n. 1–4, p. 161–168, http://dx.doi.org/10.1016/j.precamres.2009.09.006

Be'eri-Shlevin, Y., Katzir, Y., and Whitehouse, M., 2009a, Post-collisional tectonomagmatic evolution in the northern Arabian-Nubian Shield (ANS): time constraints from ion-probe U-Pb dating of zircon: Journal of the Geological Society, London, v. 166, n. 1, p. 71–85, http://dx.doi.org/10.1144/0016-76492007-169

Be'eri-Shlevin, Y., Katzir, Y., and Valley, J. W., 2009b, Crustal evolution and recycling in a juvenile continent: Oxygen isotope ratio of zircon in the northern Arabian Nubian Shield: Lithos, v. 107, n. 3–4, p. 169–184, http://dx.doi.org/10.1016/j.lithos.2008.10.001

Be'eri-Shlevin, Y., Samuel, M. D., Azer, M. K., Rämö, O. T., Whitehouse, M. J., and Moussa, H. E., 2011, The Ediacaran Ferani and Rutig volcano-sedimentary successions of the northernmost Arabian-Nubian Shield (ANS): new insights from zircon: Precambrian Research, v. 188, n. 1–4, p. 21–44, http://dx.doi.org/10.1016/j.precamres.2011.04.002

Be'eri-Shlevin, Y., Eyal, M., Eyal, Y., Whitehouse, M. J., and Litvinovsky, B., 2012, The Sa'al volcano-sedimentary complex (Sinai, Egypt): A latest Mesoproterozoic volcanic arc in the northern Arabian Nubian Shield: Geology, v. 40, n. 5, p. 403–406, http://dx.doi.org/10.1130/G32788.1

Bentor, Y. K., 1985, The crustal evolution of the Arabo-Nubian Massif with special reference to the Sinai Peninsula: Precambrian Research, v. 28, n. 1, p. 1–74, http://dx.doi.org/10.1016/0301-9268(85)90074-9

Bonin, B., 2007, A-type granites and related rocks: Evolution of a concept, problems and prospects: Lithos, v. 97, n. 1–2, p. 1–29, http://dx.doi.org/10.1016/j.lithos.2006.12.007

Bons, P. D., Arnold, J., Elburg, M. A., Kalda, J., Soesoo, A., and van Milligen, B. P., 2004. Melt extraction and accumulation from partially molten rocks: Lithos, v. 78, n. 1–2, p. 25–42, http://dx.doi.org/10.1016/j.lithos.2004.04.041

Brown, M., and Solar, G. S., 1999, The mechanism of ascent and emplacement of granite magma during transpression: a syntectonic granite paradigm: Tectonophysics, v. 312, p. 1–33, http://dx.doi.org/10.1016/S0040-1951(99)00169-9

Bruner, I., ms, 1982, The ring dike of Katherina: Beer-Sheva, Israel, Ben-Gurion University of the Negev, M. S. thesis (in Hebrew, English Abstract), 78 p.

Eyal, M., and Hezkiyahu, T., 1980, Katherina Pluton—the outlines of a petrological framework: Israel Journal of Earth Sciences, v. 29, p. 41–52.

Eyal, M., Bartov, Y., Shimron, A. E., and Bentor, Y. K., 1980, Sinai Geological Map: Jerusalem, Geological Survey of Israel, scale 1:500,000.

Eyal, M., Litvinovsky, B., Jahn, B. M., Zanvilevich, A., and Katzir, Y., 2010, Origin and evolution of post-collisional magmatism: Coeval Neoproterozoic calc-alkaline and alkaline suites of the Sinai Peninsula: Chemical Geology, v. 269, n. 3–4, p. 153–179, http://dx.doi.org/10.1016/j.chemgeo.2009.09.010

Gass, I. G., 1982, Upper Proterozoic (Pan-African) calc-alkaline magmatism in North-eastern Africa and Arabia, *in* Thorpe, R. S., editor, Andesites and related rocks: Chichester, England, John Wiley and Sons, p. 595–609.

Genna, A., Nehlig, P., Le Goff, E., Guerrot, C., and Shanti, M., 2002, Proterozoic tectonism of the Arabian Shield: Precambrian Research, v. 117, n. 1–2, p. 21–40, http://dx.doi.org/10.1016/S0301-9268(02)00061-X

Goor, A., ms, 1982, Katherina volcanics—an internal ring complex of the High Mountain, southern Sinai: Beer-Sheva, Israel, Ben-Gurion University of the Negev, M. S. thesis (in Hebrew, English Abstract), 101 p.

Farahat, E. S., and Azer, M. K., 2011, Post-collisional magmatism in the northern Arabian-Nubian Shield: The geotectonic evolution of the alkaline suite at Gebel Tarbush area, south Sinai, Egypt: Chemie der Erde—Geochemistry, v. 71, n. 3, p. 247–266, http://dx.doi.org/10.1016/j.chemer.2011.06.003

Hargrove, U. S., Stern, R. J., Kimura, J.-I., Manton, W. I., and Johnson, P. R., 2006, How juvenile is the Arabian-Nubian Shield? Evidence from Nd isotopes and pre-Neoproterozoic inherited zircon in Bi'r Umq suture zone, Saudi Arabia: Earth and Planetary Science Letters, v. 252, n. 3–4, p. 308–326, http://dx.doi.org/10.1016/j.epsl.2006.10.002

Harris, N. B. W., 1985, Alkaline complexes from the Arabian Shield: Journal of African Earth Sciences, v. 3, p. 83–88.

Jahn, B.-M., Wu, F., Capdevila, R., Martineau, F., Zhao, Z., and Wang, Y., 2001, Highly evolved juvenile granites with tetrad effect patterns; the Worduhe and Baerzhe granites from the Great Xing'an (Khingan) Mountains in NE China: Lithos, v. 59, n. 4, p. 171–198, http://dx.doi.org/10.1016/S0024-4937(01)00066-4

Jahn, B. M., Litvinovsky, B. A., Zanvilevich, A. N., and Reichow, M., 2009, Peralkaline granitoid magmatism in the Mongolian-Transbaikalian Belt: Evolution, petrogenesis and tectonic significance: Lithos, v. 113, n. 3–4, p. 521–539, http://dx.doi.org/10.1016/j.lithos.2009.06.015

James, R. S., and Hamilton, D. L., 1969, Phase relations in the system $NaAlSi_3O_8$-$KAlSi_3O_8$-$CaAl_2Si_2O_8$-SiO_2 at 1 kilobar water vapour pressure: Contributions to Mineralogy and Petrology, v. 21, n. 2, p. 111–141, http://dx.doi.org/10.1007/BF00403341

Jarrar, G., Stern, R. J., Saffarini, G., and Al-Zubi, H., 2003, Late- and post-orogenic Neoproterozoic intrusions of Jordan: implications for crustal growth in the northernmost segment of the East African Orogen: Precambrian Research, v. 123, n. 2–4, p. 295–319, http://dx.doi.org/10.1016/S0301-9268(03)00073-1

Jarrar, G. H., Manton, W. I., Stern, R. J., and Zachmann F., 2008, Late Neoproterozoic A-type granites in the northernmost Arabian-Nubian Shield formed by fractionation of basaltic melts: Chemie der Erde—Geochemistry, v. 68, n. 3, p. 295–312, http://dx.doi.org/10.1016/j.chemer.2006.09.002

Johannes, W., and Holtz, F., 1996, Petrogenesis and experimental petrology of granitic rocks: Berlin, Springer-Verlag, 330 p.

Katzir, Y., Eyal, M., Litvinovsky, B. A., Jahn, B. M., Zanvilevich, A. N., Valley, J. W., Beeri, Y., Pelly, I., and Shimshilashvili, E., 2007, Petrogenesis of A-type granites and origin of vertical zoning in the Katherina pluton, Gebel Mussa (Mt. Moses) area, Sinai, Egypt: Lithos, v. 95, n. 3–4, p. 208–228, http://dx.doi.org/10.1016/j.lithos.2006.07.013

Kelemen, P. B., Hanghøj, K., and Greene, A. R., 2007, One view of the geochemistry of subduction-related magmatic arcs, with emphasis on primitive andesite and lower crust, *in* Rudnick, R. L., editor, The Crust: Treatise of Geochemistry, v. 3, p. 1–70, http://dx.doi.org/10.1016/B0-08-043751-6/03035-8

Kovalenko, N. I., 1978, The reaction between granite and aqueous hydrofluoric acid in relation to the origin of fluorine-bearing granites: Geochemistry International, v. 14, p. 108–118.

Kovalenko, V. I., Naumov, V. B., Solovova, I. P., Girnis, A. V., Hervig, R. L., and Boriani, A., 1994, Volatiles, composition and conditions of crystallization of magmas formed basalt-pantellerite association at Pantelleria Island (by study of melt and fluid inclusions): Petrologiya, v. 2, p. 24–42. (Petrology, v. 2, p. 24–42, translated from original Russian)

Kröner, A., Greiling, R., Reischmann, T., Hussein, I. M., Stern, R. J., Durr, S., Krugger, J., and Zimmer, M., 1987, Pan-African crustal evolution in the Nubian segment of north-eastern Africa, *in* Kröner, A., editor, Proterozoic Lithospheric evolution: American Geophysical Union, Geodynanic Series, v. 17, p. 235–257, http://dx.doi.org/10.1029/GD017p0235

Küster, D., and Harms, U., 1998, Post-collisional potassic granitoids from the southern and northernwestern parts of the Late Neoproterozoic East African orogen: a review: Lithos, v. 47, n. 1–4, p. 177–195, http://dx.doi.org/10.1016/S0024-4937(98)00031-0

Kuzmin, D. V., Chupin, V. P., and Litvinovsky, B. A., 1999, Temperature and composition of magmas formed trachybasalt-comendite suite in the Tsagan-Khurtei Range, West Transbaikalia (by melt inclusions study): Russian Geology and Geophysics, v. 40, p. 62–72.

Le Maitre, R. W., editor, 1989, A Classification of Igneous Rocks and Glossary of Terms: recommendations of the International Union of Geological Sciences Subcommission on the Systematics of Igneous Rocks: Oxford, Blackwell, 193 p.

Leake, B. E., 1978, Nomenclature of amphiboles: American Mineralogist, v. 63, n. 11–12, p. 1023–1053.

Leitch, A. M., and Weinberg, R. F., 2002, Modeling granite migration by mesoscale pervasive flow: Earth and Planetary Science Letters, v. 200, p. 131–146, http://dx.doi.org/10.1016/S0012-821X(02)00596-4

Liégeois, J. P., and Black, R., 1987, Alkaline magmatism subsequent to collision in the Pan-African belt of the Adrar des Iforas *in* Fitton, J. G., and Upton, B. G. J., editors, Alkaline Igneous Rocks: Geological Society, London, Special Publications, v. 30, p. 381–401, http://dx.doi.org/10.1144/GSL.SP.1987.030.01.18

Liégeois, J. P., and Stern, R. J., 2010, Sr-Nd isotopes and geochemistry of granite-gneiss complexes from the Meatiq and Hafafit domes, Eastern Desert, Egypt: No evidence for pre-Neoproterozoic crust: Journal of African Earth Sciences 57, n. 1–2, p. 31–40, http://dx.doi.org/10.1016/j.jafrearsci.2009.07.006

Lindsley, D. H., 1983, Pyroxene thermometry: American Mineralogist, v. 18, p. 477–493.

Lindsley, D. H., and Nekvasil, H., 1989. A ternary feldspar model for all reasons: EOS, Transactions of American Geophysical Union, v. 70, p. 506.

Litvinovsky, B. A., Yarmolyuk, V. V., Vorontsov, A. A., Zhuravlev, D. Z., Posokhov, B. F., Sandimirova, G. P., and Kuzmin, D. V., 2001, Late Triassic stage of formation of the Mongolian-Transbaikalian alkaline-granitoid province: data of isotope-geochemical studies: Russian Geology and Geophysics, v. 42, p. 445–455.

Litvinovsky, B. A., Jahn, B.-m., Zanvilevich, A. N., Saunders, A., and Poulain, S., Kuzmin, D. V., Reichow, M. K., and Titov, A. V., 2002, Petrogenesis of syenite-granite suites from the Bryansky Complex (Transbaikalia, Russia): implications for the origin of A-type granitoid magmas: Chemical Geology, v. 189, n. 1–2, p. 105–133, http://dx.doi.org/10.1016/S0009-2541(02)00142-0

Litvinovsky, B. A., Karmanov, N. S., and Vapnic, E., 2006, Genesis of ultrapotassic quartz porphyry in the northern Arabian-Nubian Shield: Russian Geology and Geophysics, v. 47, p. 1123–1147.

Meert, J. G., 2003, A synopsis of events related to the assembly of eastern: Gondwana: Tectonophysics, v. 362, n. 1–4, p. 1–40, http://dx.doi.org/10.1016/S0040-1951(02)00629-7

Moghazi, A. M., Harbi, H. M., and Ali, K. A., 2011, Geochemistry of the Late Neoproterozoic Hadb adh Dayheen ring complex, Central Arabian Shield: Implications for the origin of rare-metal-bearing post-orogenic A-type granites: Journal of Asian Earth Sciences. v. 42, n. 6, p. 1324–1340, http://dx.doi.org/10.1016/j.jseaes.2011.07.018

Moreno, J. A., Montero, P., Abu Anbar, M. A., Molina, J. F., Scarrow, J. H., Talavera, C., Cambeses, A., and Bea, F., 2012, SHRIMP U-Pb zircon dating of the Katerina Ring Complex: Insights into the temporal sequence of Ediacaran calc-alkaline to peralkaline magmatism in southern Sinai, Egypt: Gondwana Research v. 21, n. 4, p. 887–900, http://dx.doi.org/10.1016/j.gr.2011.08.010

Morimoto, N., Fabries, J., Ferguson, A. K., Ginzburg, I. V., Ross, M., Seifert, F. A., and Zussman, J., 1988, Nomenclature of pyroxenes: Mineralogical Magazine, v. 52, p. 535–550, http://dx.doi.org/10.1180/minmag.1988.052.367.15

Nekvasil, H., 1992, Feldspar crystallisation in felsic magmas: a review: Geological Society of America, Special Papers, v. 272, p. 399–407, http://dx.doi.org/10.1130/SPE272-p399

Reyf, F. G., 1997, Direct evolution of W-rich brines from crystallizing melt within the Mariktikan granite pluton, west Transbaikalia: Mineral Deposita, v. 32, n. 5, p. 475–490, http://dx.doi.org/10.1007/s001260050116

——— 2004, Immiscible phases of magmatic fluid and their relation to Be and Mo mineralization at the Yermakovka F-Be deposit, Transbaikalia, Russia: Chemical Geology, v. 210, n. 1–4, p. 49–71, http://dx.doi.org/10.1016/j.chemgeo.2004.06.004

Rickwood, P. C., 1989, Boundary lines within petrologic diagrams, which use oxides of major and minor elements: Lithos, v. 22, n. 4, p. 247–263, http://dx.doi.org/10.1016/0024-4937(89)90028-5

Roedder, E., 1979, Origin and significance of melt inclusions: Bulletin de Mineralogie, v. 102, p. 487–510.

Samuel, D. M., Be'eri-Shlevin, Y., Azer, M. K., Whitehouse, M. J., and Moussa, H. E., 2011, Provenance of conglomerate clasts from the volcano-sedimentary sequence at Wadi Rutig in Southern Sinai, Egypt as revealed by SIMS U-Pb dating of zircon: Gondwana Research, v. 20, n. 2–3, p. 450–464, http://dx.doi.org/10.1016/j.gr.2010.11.021

Smith, J. V., and Brown, W. I., 1988, Feldspar minerals. Volume 1: Berlin, Springer-Verlag, 479 p.

Stern, R. J., 1994, Arc assembly and continental collision in the Neoproterozoic East African orogen: Implications for the consolidation of Gondwanaland: Annual Reviews of Earth and Planetary Sciences, v. 22, p. 319–351, http://dx.doi.org/10.1146/annurev.ea.22.050194.001535

——— 2002, Crustal evolution in the East African Orogen: a neodymium isotopic perspective: Journal of African Earth Sciences, v. 34, n. 3–4, p. 109–117, http://dx.doi.org/10.1016/S0899-5362(02)00012-X

Stern, R. J., Gottfried, D., and Hedge, C. E., 1984, Late Precambrian rifting and crustal evolution in the Northeastern Desert of Egypt: Geology, v. 12, n. 3, p. 168–172, http://dx.doi.org/10.1130/0091-7613(1984)12⟨168:LPRACE⟩2.0.CO;2

Streckeisen, A., and Le Maitre, R. W., 1979, A chemical approach to the Modal (QAPF classification of the igneous rocks: Neues Jarbuch Mineralogie, v. 136, n. 2, p. 169–206.

Sun S., and McDonough, W. F., 1989, Chemical and isotopic systematics of oceanic basalts, implications for mantle compositions and processes, *in* Saunders, A. D., and Norry, M. J., editors, Magmatism in the Ocean Basins: Geological Society, London, Special Publications, v. 42, p. 313–345, http://dx.doi.org/10.1144/GSL.SP.1989.042.01.19

Thomas, R., and Klemm, W., 1997. Microthermometry study of silicate melt inclusions in Variscan granites from SE Germany: volatile contents and entrapment conditions: Journal of Petrology, v. 38, n. 12, p. 1753–1765, http://dx.doi.org/10.1093/petroj/38.12.1753

Vail, J. R., 1989, Ring complexes and related rocks in Africa: Journal of African Earth Sciences, v. 8, n. 1, p. 19–40, http://dx.doi.org/10.1016/S0899-5362(89)80006-5

Valley, J. W., 2003, Oxygen isotopes in zircon, *in* Hanchar, J. M., and Hoskin, P. W. O., editors, Zircon: Reviews in Mineralogy and Geochemistry, v. 53, p. 343–385, http://dx.doi.org/10.2113/0530343

Valley, J. W., Kinny, P. D., Schulze, D. J., and Spicuzza, M. J., 1998, Zircon megacrysts from kimberlite: oxygen isotope variability among mantle melts: Contributions to Mineralogy and Petrology, v. 133, n. 1–2, p. 1–11, http://dx.doi.org/10.1007/s004100050432

van der Molen, I., and Peterson, M. S., 1979, Experimental deformation of partially-melt granite: Contributions to Mineralogy and Petrology, v. 70, n. 3, p. 299–318, http://dx.doi.org/10.1007/BF00375359

Vigneresse, J. L., Barbey, P., and Cuney, M., 1996, Rheological transitions during partial melting and crystallization with application to felsic magma segregation and transfer: Journal of Petrology, v. 37, n. 6, p. 1579–1600, http://dx.doi.org/10.1093/petrology/37.6.1579

Webster, J. D., and Rebbert, C. R., 2001, The geochemical signature of fluid-saturated magma determined from silicate melt inclusions in Asension Island granite xenolith: Geochimica et Cosmochimica Acta, v. 65, n. 1, p. 123–136, http://dx.doi.org/10.1016/S0016-7037(00)00515-9

Weinberg, R. F., 1999, Mesoscale pervasive felsic magma migration: alternatives to dyking: Lithos, v. 46, n. 3, p. 393–410, http://dx.doi.org/10.1016/S0024-4937(98)00075-9

Yoder, H. S., Steward, D. B., and Smith, J. R., 1957, Ternary feldspars: Carnegie Institute, Washington Year Book, v. 55, p. 206–214.